The long-time motion of vortex sheets with surface tension

T. Y. Hou
Department of Applied Mathematics, California Institute of Technology, Pasadena, California 91125

J. S. Lowengrub
School of Mathematics, University of Minnesota, Minneapolis, Minnesota 55455

M. J. Shelley
Courant Institute of Mathematical Sciences, New York University, New York, New York 10012

(Received 12 January 1996; accepted 17 March 1997)

We study numerically the simplest model of two incompressible, immiscible fluids shearing past one another. The fluids are two-dimensional, inviscid, irrotational, density matched, and separated by a sharp interface under a surface tension. The nonlinear growth and evolution of this interface is governed by only the competing effects of the Kelvin–Helmholtz instability and the dispersion due to surface tension. We have developed new and highly accurate numerical methods designed to treat the difficulties associated with the presence of surface tension. This allows us to accurately simulate the evolution of the interface over much longer times than has been done previously. A surprisingly rich variety of behavior is found. For small Weber numbers, where there are no unstable length-scales, the flow is dispersively dominated and oscillatory behavior is observed. For intermediate Weber numbers, where there are only a few unstable length-scales, the interface forms elongating and interpenetrating fingers of fluid. At larger Weber numbers, where there are many unstable scales, the interface rolls-up into a ''Kelvin-Helmholtz'' spiral with its late evolution terminated by the collision of the interface with itself, forming at that instant bubbles of fluid at the core of the spiral. Using locally refined grids, this singular event (a ''topological'' or ''pinching'' singularity) is studied carefully. Our computations suggest at least a partial conformance to a local self-similar scaling. For fixed initial data, the pinching singularity times decrease as the surface tension is reduced, apparently towards the singularity time associated with the zero surface tension problem, as studied by Moore and others. Simulations from more complicated, multi-modal initial data show the evolution as a combination of these fingers, spirals, and pinches. [S1070-6631(97)02407-0]

I. INTRODUCTION

The Kelvin–Helmholtz (K–H) instability is a fundamental instability of incompressible fluid flow at high Reynolds number, arising generally from the shearing of one fluid mass past another. If the two fluids are immiscible, then they are naturally separated by an sharp interface across which there is a surface tension. The surface tension arises from the imbalance of the two fluids' intermolecular cohesive forces, and exists even if the two fluids are density and viscosity matched. Dynamically, surface tension acts as a dispersive regularization of the K–H instability.

In this paper, we consider the simplest case. The two shearing fluids are two-dimensional, inviscid, irrotational, density matched, and separated by a sharp interface. This interface can then be described as a *vortex sheet*. That is, a surface across which there is a discontinuity in tangential velocity.[1] The nonlinear growth and evolution of this interface is governed by only the competing effects of the K–H instability and the dispersion due to surface tension. Using new numerical methods, developed partly in Hou, Lowengrub, and Shelley (HLS94),[2] we have been able to compute accurately the nonlinear evolution of this system over much larger times than previously possible. We find a surprisingly rich variety of behavior within this relatively simple framework. Using fixed initial data close to equilibrium, the ensuing evolution is studied as the Weber number We is varied. In effect, We measures the strength of the K–H instability relative to the dispersive stabilization associated with surface tension. For small We, where there are no initially unstable length scales (dispersively dominated), the interface simply oscillates in time, over tens of periods, with no apparent development of the new structure. For intermediate We, where there are now a few initially unstable length-scales, the interface forms elongating fingers that interpenetrate each fluid into the other. This is illustrated in the right box of Fig. 4. At We ten times larger, where there are many more initially unstable length-scales (K–H dominated), the interface rolls up into a ''Kelvin-Helmholtz spiral.'' However, further roll-up is terminated by the collision of the interface with itself, forming trapped bubbles of fluid at the core of the spiral. The development of this event is shown in Fig. 11. Simulations from more general initial data show the evolution as a combination of these fingers, spirals, and pinches.

The collision of material surfaces, such as the self-intersection of an interface, constitutes a singularity in the evolution, implying at least the divergence of velocity gradients (an argument for this is given in Appendix C). Here, the collision is linked intimately to the creation of intense localized jets produced by the surface tension. Our numerical results suggest that both the true vortex sheet strength (the jump in tangential velocity across the sheet), and the interfacial curvature diverge at the collision time, with the interface

apparently forming corners. Physically, this collision may signal an imminent change in the topology of the flow and so this event is referred to as a *topological* or *pinching* singularity. Of course, such events are commonly observed, with a standard example being the pinching and fissioning of three-dimensional liquid jets. However, taking an axially symmetric, inviscid jet as a prototype, the pinching occurs through the nonlinear development of the classical Rayleigh instability,[3] itself driven strongly by the azimuthal component of the surface tension contribution. This component is completely absent in a two-dimensional flow, making the appearance of such pinching singularities more surprising.

Because of its technological and scientific importance, understanding the motion of interfaces that bound masses of fluid undergoing fission has become an area of intense research activity. A small sampling of recent studies includes work in Stokes flows,[4,5] lubrication models of thin-film and Hele–Shaw flows,[6–9] Hele–Shaw flows,[10,8,11] and shallow water approximations and experiments of axially symmetric jets.[12–14] Of particular relevance here, Keller and Miksis[15] have given an asymptotic analysis of the immediate aftermath of a topological transition occurring when a tapered, infinite layer of inviscid, incompressible fluid (surrounded by air) breaks into two semi-infinite, finite-angled fluid wedges. Supposing that the layer breaks at time $t=0$, Keller and Miksis use a similarity analysis to find the resulting flow velocity and gap width for $t>0$. They find that the flow velocity is initially infinite and decays in time like $(t\rho/\tau)^{-1/3}$ where ρ is the density of the fluid. The gap width grows like $(t\sqrt{\tau/\rho})^{2/3}$. Their work does not apply directly to our observed pinching singularity since in our case fluid is on both sides of the self-intersecting interface. This introduces a further, nontrivial nonlocality to the problem. Moreover, rather than exiting a topological transition, our system is approaching one. Nevertheless, our equations can be recast in self-similar variables using these temporal exponents and as will be described in Sec. IV, our numerical results suggest at least partial agreement with the temporal exponents of Keller and Miksis.

The behavior of vortex sheets in the absence of surface tension is much different. In this case, $We=\infty$ and the unregularized K–H instability produces infinitely many unstable scales. It is now well known that the interface develops isolated singularities that are not associated with any large-scale structure of the sheet such as roll-up. In an asymptotic analysis valid for initial data close to equilibrium, Moore[16] gave the first analytical evidence for this singularity. Moore's analysis suggests that at the time $t=t_M$, the interface profile, while still being nearly flat, acquires isolated square-root singularities in its curvature. Moreover, the true vortex sheet strength remains finite at $t=t_M$, but does develop a cusp that is associated with a rapid compression of circulation in the neighborhood of the singularity. The $We=\infty$ singularity is hereafter referred to as the *Moore singularity*.

Caflisch and Orellana[17] later reinterpreted Moore's analysis and presented a class of ''exact'' solutions to the full nonlinear equations. The Caflisch and Orellana solutions, of which Moore's is one case, develop singularities at finite times. Numerical computations performed by Meiron, Baker, and Orszag,[18] Krasny,[19] and particularly Shelley,[20] suggest that the generic singularity structure is given by the analysis of Moore. In the absence of surface tension, Moore's analysis was extended to the Boussinesq problem by Pugh[21] and to the full Rayleigh–Taylor problem by Baker, Caflisch, and Siegel[22] (also see Ref. 23).

We do not observe the Moore singularity in the presence of surface tension, though at large We its shadow is seen by the rapid production of dispersive waves. While a topological singularity is observed at late times, it is of a fundamentally different type than the Moore singularity. Rather than occurring through the rapid *compression* of circulation as in the Moore singularity, the topological singularity is associated with the rapid *production* of new, localized circulation.

Siegel[24] has recently extended Moore's analysis to the nonzero surface tension case (i.e., $We<\infty$). Using a special initial condition, Siegel constructs travelling wave solutions to a reduced system of equations. Siegel's analysis predicts the formation of finite time singularities whenever there is at least one linearly unstable Fourier mode. The predicted structure of the singularity, however, is quite different from that observed in our numerical simulations. This is further discussed in the Conclusion.

Because an analysis of the full vortex sheet equations in the presence of surface tension is so difficult, most of the previous studies of surface tension effects have been numerical. Still, it has been problematic to pose stable numerical methods, even in the semi-discrete case where time is not discretized. Many numerical methods treat the small scales incorrectly, either through the introduction of aliasing errors or by artificial smoothing. This can lead to numerical instabilities that are related to the K–H instability.[25–27] Examples of this are seen in the computations of Zalosh[28] and Pullin.[29] In independent works, Baker and Nachbin[25] and Beale, Hou, and Lowengrub[26,27] identified the source of numerical instability in these surface tension computations and gave alternative, stable numerical methods.

Additional difficulties occur when fully discrete methods are considered. Surface tension introduces high-order spatial terms through the interface curvature appearing in the Laplace–Young boundary condition. These terms appear nonlocally in the equations of motion due to the incompressibility constraint, and are nonlinear functionals of the sheet position due to their origin in the curvature. These terms create dispersion in the dynamics and are dominant at small length-scales. For explicit time-stepping methods, this introduces high-order time-step stability constraints that depend on the spatial resolution. We refer to such constraints as ''stiffness.'' These constraints can be made more severe by the differential clustering of grid points along the interface. For example, if the ''Lagrangian'' formulation and explicit time stepping were used (as in Refs. 29,30,25,26) to calculate the interface evolution shown in Fig. 11, then the stability bound on the time step, for a fixed spatial resolution, would decrease by a factor of 10^6 over the course of the simulation.

Rangel and Sirignano[30] attempt to circumvent these difficulties by using a redistribution algorithm that reparam-

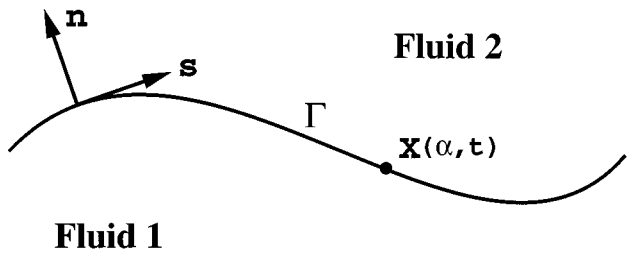

FIG. 1. A schematic of the fluid interface problem.

etrizes the interface uniformly in arclength after each time step. This keeps points from clustering, but as a result of repeated interpolations, it has also a strong smoothing effect on the sheet. This yields results that disagree on several points with other work. For example, Rangel and Sirignano are able to compute the roll-up of a vortex sheet *without* surface tension, with an accompanying divergence of the true vortex sheet strength. This is in direct contradiction to the results of Moore,[16] and its associated, very accurate numerical studies.[18–20]

The numerical results presented in this paper rely on numerical methods, designed for handling surface tension, that were developed in part in HLS94. In HLS94, we presented a different formulation for computing the motion of fluid interfaces with surface tension in two-dimensional, irrotational and incompressible fluids. This formulation has all the nice properties for time integration methods that are associated with having a linear highest-order term. The resulting numerical methods do not have the severe stability constraints usually associated with surface tension. Our approach was based on a boundary integral formulation[31] and was applied in HLS94 to Euler and Hele–Shaw flows. Our approach applies more generally, though, even to problems beyond the fluid mechanical context. In the study of the topological singularity presented in this paper, we additionally incorporate local grid refinement and use a 4th-order time-stepping method to achieve increased spatial and temporal accuracy.

The organization of the paper is as follows. In Section II, a boundary integral formulation is given for the motion of fluid interfaces under surface tension in two-dimensional Euler flows. In Section III, the numerical methods are briefly outlined. Many further details of implementation are found in HLS94. Extensions to the work in HLS94 — a high-order time-integration method and an implementation of local grid refinement — are found in Appendices A and B. The results of numerical simulations are presented in Section IV. Concluding remarks are given in Section V.

II. THE EQUATIONS OF MOTION

Consider two inviscid, incompressible, and irrotational fluids separated by the parametrized planar interface Γ given by $\mathbf{X}(\alpha)=(x(\alpha),y(\alpha))$, as shown schematically in Fig. 1. The lower fluid is denoted 1, and the upper fluid is denoted 2. $\hat{\mathbf{n}}$ and $\hat{\mathbf{s}}$ are respectively the unit normal and tangent vectors to Γ, while κ is its curvature. For simplicity, the density is assumed to be constant on each side of Γ. Here, the velocity on either side of Γ is evolved by the incompressible Euler equations,

$$\mathbf{u}_{j_t}+(\mathbf{u}_j\cdot\nabla)\mathbf{u}_j=-\frac{1}{\rho_j}\nabla(p_j+\rho_j g y),\quad \nabla\cdot\mathbf{u}_j=0, \tag{1}$$

where the subscript j denotes the upper or lower fluid. There are the boundary conditions,

$$(i)\ \ [\mathbf{u}]_\Gamma\cdot\hat{\mathbf{n}}=0,\ \text{the kinematic boundary condition,} \tag{2}$$

$$(ii)\ \ [p]_\Gamma=\tau\kappa,\ \text{the Laplace–Young boundary condition,} \tag{3}$$

$$(iii)\ \ \mathbf{u}_j(x,y)\to(\pm V_\infty,0)\ \text{as}\ y\to\pm\infty,\ \text{the far - field boundary condition.} \tag{4}$$

Here, $[\,\cdot\,]_\Gamma$ denotes the jump taken from above to below Γ. The tangential component of fluid velocity is typically discontinuous at Γ. Such an interface is called a **vortex sheet** (see Ref. 1). The velocity at a point $\mathbf{X}$ away from the interface has the integral representation

$$\mathbf{u}(\mathbf{X})=\frac{1}{2\pi}\int\gamma(\alpha')\frac{(\mathbf{X}-\mathbf{X}(\alpha'))^\perp}{|\mathbf{X}-\mathbf{X}(\alpha')|^2}d\alpha', \tag{5}$$

where $\mathbf{X}^\perp=(-y,x)$. γ is called the (unnormalized) vortex sheet strength. It gives the velocity difference across Γ by

$$\tilde{\gamma}=\frac{\gamma(\alpha)}{s_\alpha}=[\mathbf{u}]|_\Gamma\cdot\hat{\mathbf{s}}, \tag{6}$$

where $s_\alpha=\sqrt{x_\alpha^2+y_\alpha^2}$ is the arclength metric. The velocity jump $\tilde{\gamma}$ is called the true vortex sheet strength. This representation is well known; see Ref. 31. We will consider flows that are 1-periodic in the x-direction. The average value, $\overline{\gamma}$, of γ over a period in α satisfies $-\overline{\gamma}/2=V_\infty$.

While there is a discontinuity in the tangential component of the velocity at Γ, the normal component, $U(\alpha)$, is continuous and is given by Eq. (5) as

$$U(\alpha)=\mathbf{W}(\alpha)\cdot\hat{\mathbf{n}} \tag{7}$$

where

$$\mathbf{W}(\alpha)=\frac{1}{2\pi}P.V.\int\gamma(\alpha')\frac{(\mathbf{X}(\alpha)-\mathbf{X}(\alpha'))^\perp}{|\mathbf{X}(\alpha)-\mathbf{X}(\alpha')|^2}d\alpha', \tag{8}$$

and $P.V.$ denotes the principal value integral. This integral is called the Birkhoff–Rott integral.

Using the representation (5) of the velocity, Euler's equation at the interface, and the Laplace–Young condition, the equations of motion for the interface are

$$\mathbf{X}_t=U\hat{\mathbf{n}}+T\hat{\mathbf{s}}, \tag{9}$$

$$\begin{aligned}\gamma_t&-\partial_\alpha((T-\mathbf{W}\cdot\hat{\mathbf{s}})\gamma/s_\alpha)\\&=-2A_\rho(s_\alpha\mathbf{W}_t\cdot\hat{\mathbf{s}}+\tfrac{1}{8}\partial_\alpha(\gamma/s_\alpha)^2-(T-\mathbf{W}\cdot\hat{\mathbf{s}})\mathbf{W}_\alpha\cdot\hat{\mathbf{s}}/s_\alpha)\\&\quad-Fr^{-1}y_\alpha+We^{-1}\kappa_\alpha.\end{aligned} \tag{10}$$

Here, the equations have been nondimensionalized on a periodicity length λ (so that the nondimensional period length is 1) and the velocity scale $\overline{\gamma}$, and

$$A_\rho = \frac{\Delta\rho}{2\overline{\rho}} \text{ is the Atwood ratio ,} \tag{11}$$

$$Fr = \frac{\overline{\rho\,\gamma^2}\lambda^2}{g(\Delta\rho)\lambda^3} \text{ is the Froude number,} \tag{12}$$

and

$$We = \frac{\overline{\rho}\lambda^2\overline{\gamma^2}}{\tau\lambda} \text{ is the Weber number,} \tag{13}$$

where $\Delta\rho = \rho_1 - \rho_2$, and $\overline{\rho} = (\rho_1+\rho_2)/2$. The Froude number measures the relative importance of inertial forces (the K–H instability) to gravitational forces (the Rayleigh–Taylor instability), while the Weber number measures the relative importance of inertial forces to surface tension forces (dispersion). T is an (as yet) arbitrary tangential velocity that specifies the motion of the parametrization of Γ. The so-called *Lagrangian formulation* corresponds to choosing the tangential velocity of a point on the interface to be the arithmetic average of the tangential components of the fluid velocity on either side. That is, choosing $T = \mathbf{W}\cdot\hat{\mathbf{s}}$, in which case Eq. (10) simplifies considerably.

Equation (10) is a Fredholm integral of the second kind for γ_t due to the presence of γ_t in $\mathbf{W}_t$. This equation has a unique solution, and is contractive.[31] The mean of γ is preserved by Eq. (10) and must be chosen initially to be $-2V_\infty$, to guarantee that the far-field condition (*iii*) is satisfied. Further, while γ is evolved as an independent variable, it cannot be interpreted independently of the parametrization. From Eq. (6), it is the ratio $\tilde{\gamma} = \gamma/s_\alpha$ that has a physical interpretation, and s_α is determined by the choice of T.

In this work, we study the simpler case when the two fluids are density matched, that is $A_\rho = 0 = Fr^{-1}$. The problem is then completely characterized by the Weber number, and the Lagrangian formulation of the equations of motion becomes simply

$$\mathbf{X}_t(\alpha,t) = \mathbf{W}(\alpha,t), \tag{14}$$

$$\gamma_t(\alpha,t) = We^{-1}\kappa_\alpha. \tag{15}$$

The Lagrangian formulation is characterized by an elegant compactness of statement. However, as we demonstrate in Section III, it is not a good formulation for simulation due to a differential clustering of computational points that leads to severe time-step constraints in the presence of surface tension.

A. The energy

There are several invariants of the motion — the mean and y-moment of γ, the means of x and y, and the energy. Of these invariants only the energy, through the interfacial energy, contains an explicit contribution from the presence of surface tension. Further, of these invariants, the energy is the best indicator of accuracy. It is not conserved explicitly by our numerical methods, and is a nontrivial constant of the motion.

Neither the total interfacial energy, nor the kinetic energy over a period, is finite. However, both have finite parts that together form a single invariant. The conserved (perturbation) energy $E(t)$ is the sum of the perturbation kinetic and the perturbation interfacial energies given by

$$E(t) = E_L(t) + E_K(t), \tag{16}$$

where

$$E_L(t) = We^{-1}(L-1)$$

is the perturbation interfacial energy, (17)

$$E_K(t) = \frac{1}{2}\int_0^1 \psi(\alpha',t)\,\gamma(\alpha',t)\,d\alpha'$$

is the perturbation kinetic energy. (18)

Here L is the length of Γ over a single period, and ψ is the stream function

$$\psi(\alpha,t) = -\frac{1}{2\pi}\int_0^1 \gamma(\alpha',t)\log|\sin\,\pi(z(\alpha,t) - z(\alpha',t))|\,d\alpha', \tag{19}$$

where $z(\alpha,t) = x(\alpha,t) + iy(\alpha,t)$. The formula for ψ can be rewritten, by explicitly subtracting off the logarithmic singularity and integrating by parts, to yield an expression that can be computed numerically with spectral accuracy. See Pullin[29] and Baker and Nachbin[25] for details.

B. The linear behavior

Consider first the linearized motion about the flat equilibrium, with $x(\alpha,t) = \alpha + \epsilon\xi(\alpha,t)$, $y(\alpha,t) = \epsilon\eta(\alpha,t)$, and $\gamma(\alpha,t) = 1 + \epsilon\omega(\alpha,t)$, with $\epsilon \ll 1$. For definiteness, the Lagrangian frame $T = \mathbf{W}\cdot\hat{\mathbf{s}}$ is taken. The linearized system reduces to a single equation for the vertical amplitude η,

$$\eta_{tt} = -\frac{1}{4}\eta_{\alpha\alpha} + \frac{We^{-1}}{2}H\,[\eta_{\alpha\alpha\alpha}]. \tag{20}$$

H is the Hilbert transform,[32] and is diagonalizable by the Fourier transform as $\hat{H}[f] = -i\,\mathrm{sgn}(2\pi k)\hat{f}$. The growth rate for perturbations about the flat equilibrium is given by

$$\sigma_k^2 = (2\pi)^2\left(\frac{1}{4}k^2 - 2\pi\frac{We^{-1}}{2}|k|^3\right). \tag{21}$$

The dispersion relation gives instability for wavenumbers $0 < |k| < We/4\pi$, and dispersion for wavenumbers $|k| > We/4\pi$. The wavenumber of maximum growth is $|k| = We/6\pi$. The surface tension dispersively controls the Kelvin–Helmholtz instability at large wavenumbers.

A more general linear analysis has been given by Beale, Hou and Lowengrub.[33] By linearizing around the time-dependent vortex sheet $\Gamma = (x(\alpha,t), y(\alpha,t))$ with strength $\gamma(\alpha,t)$, Beale *et al.* find the *dominant* behavior for η, now the *normal* component of the perturbation, to be

$$\eta_{tt} = -\frac{\gamma^2}{4s_\alpha^4}\eta_{\alpha\alpha} + \frac{We^{-1}}{2s_\alpha^3}H\,[\eta_{\alpha\alpha\alpha}]. \tag{22}$$

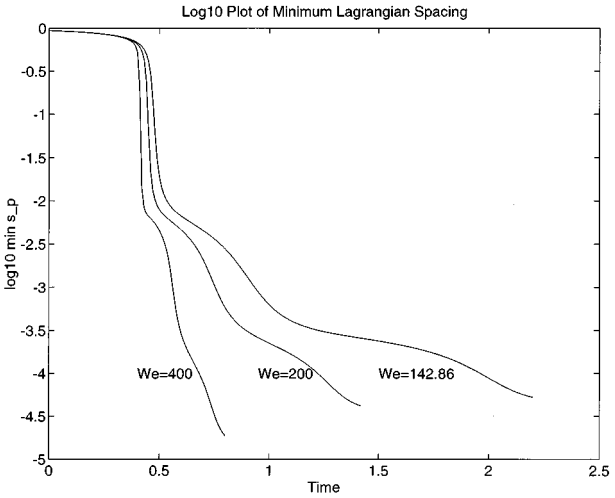

FIG. 2. The evolution of $\log_{10}(\overline{s_\alpha})$ for several Weber numbers.

The perturbation in γ has been eliminated, to leading order, by using two time derivatives on η. The same competition of effects is observed in this more general variable coefficient setting.

III. THE SMALL-SCALE DECOMPOSITION AND NUMERICAL METHODS

The primary impediment to performing long time computations of vortex sheets with surface tension is the severe time-dependent stability restriction — stiffness — imposed by the surface tension through the κ_α term appearing in Eq. (15). This is seen easily by a ''frozen coefficient'' analysis of Eq. (22). This reveals that the least restrictive time-dependent stability constraint on a stable *explicit* time integration method is

$$\Delta t < CWe^{1/2}\cdot(\overline{s_\alpha}h)^{3/2}, \quad \text{where } \overline{s_\alpha}=\min_\alpha s_\alpha, \tag{23}$$

where $h=1/N$ is the grid spacing, with N the number of points describing Γ. Since arclength spacing, Δs, satisfies $\Delta s \approx s_\alpha h$, Eq. (23) implies that the stability constraint is in fact determined by the *minimum* spacing in *arclength* between adjacent points on the grid. This can be strongly time dependent. For example, our experience is that motion in the Lagrangian frame [Eqs. (14) and (15)] leads to ''point clustering'' and hence to very stiff systems, even for flows in which the interface is smooth and the *We* is large. For several ''typical'' simulations (differing Weber numbers) discussed in the next section, Fig. 2 shows the evolution of $\overline{s_\alpha}$ associated with the Lagrangian formulation, on a base-ten logarithmic scale. This figure was not generated by computing in the Lagrangian frame, but rather by using the methods described below, and evolving a mapping to the Lagrangian frame. Over the times shown, $\overline{s_\alpha}$ decreases in value by a factor of 10^4 or more. Consequently, the time-step constraint (23) decreases by at least a factor of 10^6, even for a fixed spatial grid size h. The steep drop at slightly less than $t=0.5$ is the result of the compression associated with the shadow of the Moore singularity, which occurs at $t_M \approx 0.37$ for this initial data.[19] Such strongly time-dependent time-step constraints have severely limited previous numerical investigations.

The primary challenge to computing the long time evolution of interfacial flows with surface tension lies in the construction of time integration methods with good stability properties. It is difficult to straightforwardly construct efficient implicit time integration methods as the source of the stiffness — the κ_α in the γ-equation — involves both a nonlinear combination of high derivatives of the interface position and contributes nonlocally to the motion through the γ in the Birkhoff–Rott integral. Our approach, first given in HLS94, involves reformulating the equations of motion according to the following three steps: **(A)** $\theta - s_\alpha$ formulation; **(B)** small scale analysis; **(C)** special choices of reference frames (tangential velocities).

(A) $\theta - s_\alpha$ formulation

Rather than using x,y as the dynamical variables, repose the evolution in variables that are more naturally related to curvature. Motivated by the identity $\theta_s=\kappa$, where θ the tangent angle to the curve Γ, the evolution is formulated with θ and s_α as the independent dynamical variables (see Whitham[34] for an early application). The equations of motion are then given by

$$s_{\alpha t} = T_\alpha - \theta_\alpha U, \tag{24}$$

$$\theta_t = \frac{1}{s_\alpha}U_\alpha + \frac{T}{s_\alpha}\theta_\alpha, \tag{25}$$

$$\gamma_t = We^{-1}\partial_\alpha(\theta_\alpha/s_\alpha) + \partial_\alpha((T-\mathbf{W}\cdot\hat{\mathbf{s}})\gamma/s_\alpha). \tag{26}$$

Given s_α and θ, the position $(x(\alpha,t),y(\alpha,t))$ is reconstructed up to a translation by direct integration of

$$(x_\alpha, y_\alpha) = s_\alpha(\cos(\theta(\alpha,t)), \sin(\theta(\alpha,t))), \tag{27}$$

which defines the tangent angle. The integration constant is supplied by evolving the position at one point $\mathbf{X}_0(t)$.

(B) Small-scale analysis

Reformulate the equations by explicitly separating the dominant terms at small spatial scales. The behavior of the equations at small scales is important because stability constraints (i.e., stiffness) arise from the influence of high-order terms *at small spatial scales*. In HLS94 we show that at small scales the Birkhoff–Rott operator simplifies enormously. A useful notation, $f \sim g$, is introduced to mean that the difference between f and g is smoother than f and g. In HLS94 we show that

$$U(\alpha,t) \sim \frac{1}{2s_\alpha}H[\gamma](\alpha,t). \tag{28}$$

That is, at small spatial scales, the normal (physical) velocity is essentially the Hilbert transform with a variable coefficient. Now, Eq. (28) allows a rewriting of the equations of motion in a way that separates the dominant terms at small scales (these terms determine the stability constraints):

$$\theta_t = \frac{1}{2}\frac{1}{s_\alpha}\left(\frac{1}{s_\alpha}H[\gamma]\right)_\alpha + P, \tag{29}$$

$$\gamma_t = We^{-1}\left(\frac{\theta_\alpha}{s_\alpha}\right)_\alpha + Q. \tag{30}$$

Here, P and Q represent ''lower-order'' terms at small spatial scales. This is the *small-scale decomposition* (SSD). Assuming that s_α is given, the dominant small-scale terms are linear in θ and γ, but also nonlocal and variable coefficient. At this point, it is possible to apply standard implicit time integration techniques where the leading-order ''linear'' terms are discretized implicitly. However, we have not yet taken any advantage in choosing the tangential velocity T. There are choices of T that are especially convenient in constructing efficient time integration methods and in maintaining the accuracy of the simulations.

(C) Special choices for *T*

Choose the tangential velocity T to preserve dynamically a specific parametrization, up to a time-dependent scaling. In particular, require that

$$s_\alpha(\alpha,t) = R(\alpha)L(t), \text{ with} \int_0^1 R(\alpha)d\alpha = 1, \tag{31}$$

where $R(\alpha)$ is a given smooth and positive function. The length $L(t)$ evolves by the ODE[2]

$$L_t = -\int_0^1 \theta_{\alpha'} U d\alpha'. \tag{32}$$

If the constraint (31) is satisfied at $t=0$, then it is also satisfied dynamically in time by choosing T as

$$T(\alpha,t) = T(0,t) + \int_0^\alpha \theta_{\alpha'} U d\alpha' - \int_0^\alpha R(\alpha')d\alpha' \cdot \int_0^1 \theta_{\alpha'} U d\alpha', \tag{33}$$

where the integration constant $T(0,t)$ is typically set to zero.

We use different choices for R, and so for T. That which is computationally most convenient is $R\equiv 1$, yielding what is referred to as the uniform parametrization frame since a uniform discretization in α is then uniform in s, i.e. $s(\alpha,t)=\alpha L(t)$. In this case, the leading-order terms of small-scale decomposition, Eqs. (29) and (30), are constant coefficients in space, and implicit treatments in time of these terms are directly inverted by the Fourier transform (see Ref. 2).

Since the uniform parametrization frame keeps computational points equally spaced in arclength everywhere along the curve, this frame can be deficient in capturing structures such as the blow-up in curvature that apparently occurs in the topological singularity. From Eq. (31), if $R<1$ in such a region, then there is a greater relative concentration of grid points there. Accordingly, a nontrivial mapping R is used to cluster computational points in regions of the curve where local refinement is needed, yielding the *variable parametrization frame*. The regions where local refinement is necessary are identified beforehand by examination of simulations using the uniform parametrization. Our specific choice of R is given in Appendix A; an additional class of reference frames is also given in Appendix 2 of HLS94.

Although the possibility of using nontrivial R was discussed in HLS94, only the trivial choice $R\equiv 1$ was implemented. For a nontrivial R, the leading-order terms in the PDEs for θ and γ are still linear, but are variable coefficients in space. After an implicit treatment of these terms in Eqs. (29) and (30), the resulting time-discrete equations may be solved as follows

(i) The ODE (32) for L can be solved by an explicit method, and so its value is available at the new time-step.

(ii) An implicit treatment of the leading-order terms in the PDEs (29) and (30) leads to a linear integro-differential equation for θ at the next time-step, having the form

$$R(\alpha)\theta(\alpha) - C\left(\frac{1}{R(\alpha)}H\left[\frac{\theta_\alpha}{R}\right]_\alpha\right)_\alpha = A(\alpha),$$

where C, $R(\alpha)$, and $A(\alpha)$ are known, in part by virtue of **(i)**. The linear operator on θ is symmetric and positive definite, and the equation is solved efficiently for θ through iteration using a preconditioned conjugate gradient method. Using pseudo-spectral collocation to evaluate the linear operator, this iteration costs only $O(N\ln N)$ per step, and typically converges in a few steps. An implicit discretization of the full equations of motion would typically involve the much more expensive evaluation of the Birkhoff–Rott integral [$O(N^2)$ using direct summation] within an iteration scheme. Details on the implementation are found in Appendix B.

The extra difficulty in solving for the updated solution by iteration motivates us to use the variable parametrization frame only when it is crucial to obtain extra accuracy locally, such as is the case at late times in the regions where (topological) singularities occur.

The use of the uniform or variable parametrization frames alone, without the $\theta - s_\alpha$ reformulation and an implicit treatment of the equations of motion, does in fact prevent s_α from becoming small as s_α now scales with the overall length of Γ. This removes the strong time-dependency in time-step restriction (23). However, the 3/2-order constraint relating the time-step to the spatial grid size still remains. By using the $\theta - s_\alpha$ reformulation and the implicit treatment of the leading-order terms, this higher-order constraint is removed as well, typically leaving only a first-order Courant–Friedrichs–Lewy (CFL) type constraint from advection terms, appearing in both the θ and γ equations, that are hidden in P and Q.

In the uniform parametrization frame, we use either the 2nd-order accurate Crank–Nicholson time discretization given in HLS94 or the 4th-order accurate implicit, multi-step method due to Ascher, Ruuth, and Wetton.[35] The 4th-order method is discussed in Appendix B. In the variable parametrization frame, only the 4th-order time integration method is used. It is found in practice that a first-order CFL time step constraint (as described above) must be satisfied.

Spectrally accurate spatial discretizations are used in both the uniform and variable parametrization frames. Any differentiation, partial integration, or Hilbert transform is found at the mesh points by using the discrete Fourier transform. A spectrally-accurate, alternate-point discretization[36,20] is used to compute the velocity of the interface from Eq. (8). As noted in HLS94, time-stepping methods for vortex sheets suffer from aliasing instabilities since they are not naturally damping at the highest modes. The instability is controlled by using Fourier filtering to damp the highest modes; this determines the overall accuracy of the method, and gives a formal accuracy of $O(h^{16})$. An infinite-order filter could have been used, but we did not do so.

Again, these methods are discussed further in the Appendices and especially in HLS94. Hou and Ceniceros[37] have recently proved convergence of a SSD based formulation for vortex sheet evolution. In their work, the system is discretized in space, and continuous in time. Their analysis includes the effects of Fourier filtering, and indeed shows its sufficiency in achieving a good stability bound.

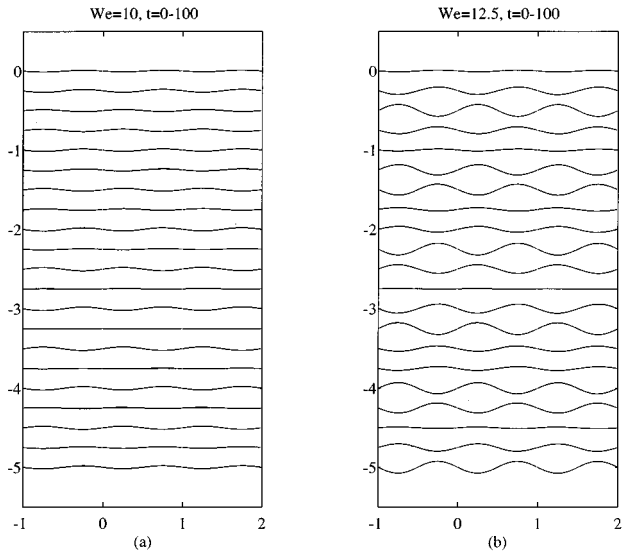

FIG. 3. The long-time evolution from initial data (34), with $We=10$ (left) and 12.5 (right). Three spatial periods are shown every 5 time units.

IV. NUMERICAL RESULTS

In the bulk of this section, we study the effect of varying the Weber number upon the evolution of the sheet from a single, fixed, near equilibrium initial condition. In particular, we consider the initial data,

$$x(\alpha,0)=\alpha+0.01\sin 2\pi\alpha, \quad y(\alpha,0)=-0.01\sin 2\pi\alpha,$$
$$\gamma(\alpha,0)=1.0, \tag{34}$$

used by Krasny[19] to study numerically the Moore singularity ($We=\infty$). He found that a curvature singularity forms at $\alpha=1/2$ ($x=1/2$) at $t_M\approx 0.37$. The singularity time and structure were in approximate agreement with Krasny's extension of Moore's analysis to this initial data. For $We<\infty$, this is not a pure eigenfunction (as it is for $We=\infty$), but is rather a combination of eigenfunctions, both stable and unstable, for the linearized evolution. The true vortex sheet strength, $\tilde{\gamma}$, is not initially constant, but instead has a single maximum in the period at $\alpha=1/2$. Finally, initial data (34) is for the Lagrangian formulation, and is recast into the uniform parametrization to set initial data for our numerical method.

At the end of this section more general initial data is considered. This includes multi-modal initial data, and data with random amplitudes and phases. Moreover, of the simulations presented in this section, only the $We=200$ case uses the fourth-order accurate time-stepping scheme and the variable parametrization frame. All other We simulations utilize the second-order Crank–Nicholson time-stepping scheme given in HLS94 and the uniform parametrization frame.

A. Small *We*

The small amplitude, small Weber number behavior is quite predictable by linear theory, even over long times. As seen from Eq. (21), there are no unstable linear modes for $We<4\pi\approx 12.56$. For $We=10$ and 12.5, the upper boxes of Fig. 3 show the computed interface positions over 3 periods every 5 time units, from $t=0$ up to $t=100$. Time increases moving down the figure. For $We=10$, all allowed wavenumbers are neutrally stable and dispersive, and the period of oscillation for the $k=1$ mode is $\omega\approx 3.95$. To the final time shown (25 periods), the motion is very well described by the linear behavior. Indeed, oscillatory behavior seems dominant, even very close to the stability threshold, as the $We=12.5$ results indicate. The impression of standing wave behavior was reinforced by examination of the maximum amplitude and interfacial energy for these two cases, which we do not show here.

We had hoped to see some repartition of energy from the $k=1$ mode to smaller scales over large times. However, for $We=10.0$ only a very slow increase is observed, if any, of the width of the active spatial spectrum. Initially, 8–9 modes are required to resolve the data to Fourier amplitudes of order 10^{-12}. By $t=1000$ (250 periods) this had increased by only 2 modes.

These calculations use $N=64$ points and time-step $\Delta t=10^{-3}$. Increasing the spatial resolution gives no change in the results. The total energy E is conserved over this time, in both cases, to a relative error of 10^{-8}. For $We=10$, the time-stepping errors were checked directly by halving the time-step and again running to $t=1000$. The error in total energy decreased by a factor of four, consistent with the Crank–Nicholson integration being of second-order accuracy. The pointwise error in θ was estimated by assuming that time-stepping error is dominant, and of second-order. Then the maximum, relative time-stepping error is approximated by

$$E_{\Delta t}=\frac{4}{3}\max_{\alpha_j}|\theta_{\Delta t}(\alpha_j,t)-\theta_{\Delta t/2}(\alpha_j,t)|/|\theta_{\Delta t}(\alpha_j,t)|.$$

This error increases slowly but steadily in time; at $t=0.1$ the error is approximately 1×10^{-4} while at $t=1000$ the error is approximately 2×10^{-3}. The pointwise error in γ and the error in L are about of the same magnitude. These results suggest that the energy is much less sensitive than the point-

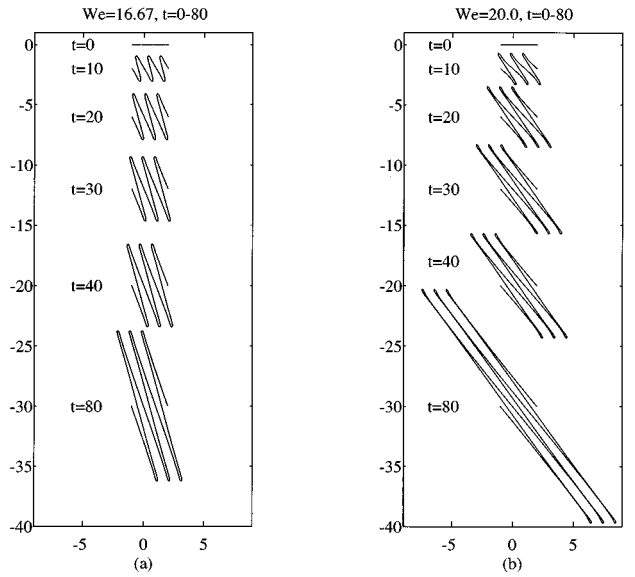

FIG. 4. Growing fingers of interpenetrating fluid for $We=16.67$ and 20. Again, three spatial periods are shown at each time.

wise data θ to errors in the time integration. Given that the motion here is very nearly linear, these errors should be mostly dispersive in nature.

B. Intermediate *We*

The evolution is much more interesting for intermediate We where the interface is initially unstable to only a few modes. Figure 4 shows the temporal behavior for two Weber numbers, $We=16.67$ and $We=20$, from $t=0$ to 80 over 3 spatial periods. In both cases, only the $k=1$ mode is linearly unstable; the $k=2$ mode becomes unstable only for $We>25$. The evolution of the interfaces is striking. The interface now deforms into elongated fingers that penetrate each fluid into the other. Lengthening, the interface acquires the shape of a blunted needle or finger, with a small pocket of fluid at its end. While the linear analysis is a rough guide, we have not sought to pinpoint the Weber number at which this transition from oscillation to growth occurs; this value is undoubtedly a function of the initial data.

For these two values of Weber number, the maximum amplitude and interfacial energy E_L follow one another closely. The growth of E_L appears to become linear in time, and lies generally below the prediction of linear theory, which predicts exponential growth. As the total energy is conserved, the perturbation kinetic energy of the fluid shows a corresponding decrease. Nothing is seen here that indicates an eventual halt to the lengthening. If the perturbation kinetic energy were a strictly positive quantity, then the interfacial energy (and so the length) could be bounded from above. However, the perturbation kinetic energy is not signed and so no such conclusion can be made.

As the fingers lengthen, they also thin. This feature does not follow from mass conservation arguments, as the mass of each fluid is infinite. Given the behavior at larger Weber numbers, it seems possible that the sides of the fingers might also collide at some finite time, and so abbreviate their

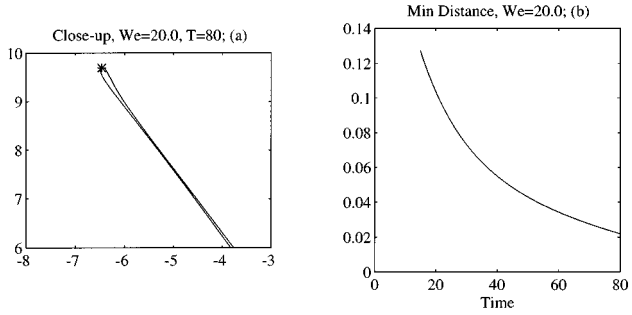

FIG. 5. A close-up of the finger tip (left box). The $\times$ denotes the point of maximum sheet strength. The right box shows the neck width of the finger as a function of time.

smooth evolution. This does not appear to be the case, at least for this initial data over these times, as Fig. 5 makes clear. For $t=80$ the left box shows a close-up of the tip region and its pocket of fluid. The neck below the tip is becoming thinner in time. The right box of the figure shows the minimum width of the neck as a function of time. So far as can be discerned, it seems that the neck is thinning exponentially, and that the neck is a stable feature of the flow; perhaps the neck is convectively stabilized by the stretching of the interfaces.

For $We=20$, Fig. 6 shows the true vortex sheet strength $\tilde{\gamma}(\alpha,t)$, over one period, at the same times as shown in Fig. 4. This figure shows that the finger lengthening is associated with the fluxing of fluid into the finger, and with the formation of a concentrated peak of positive circulation at the tip of the finger. The right peak's location is indicated by the cross on the interface close-up of Fig. 5. To the left and right of this peak, and so on the lower and upper sides of the neck, $\tilde{\gamma}$ is positive and negative, respectively. This indicates an influx of fluid from below, into the finger lengthening upwards. At the tip of every finger, there is a concentration of positive $\tilde{\gamma}$. Taken alone, these ''vortices'' might be expected to induce a rotation in the angle of inclination of the array of fingers, by the mutual induction of the upper and lower lines

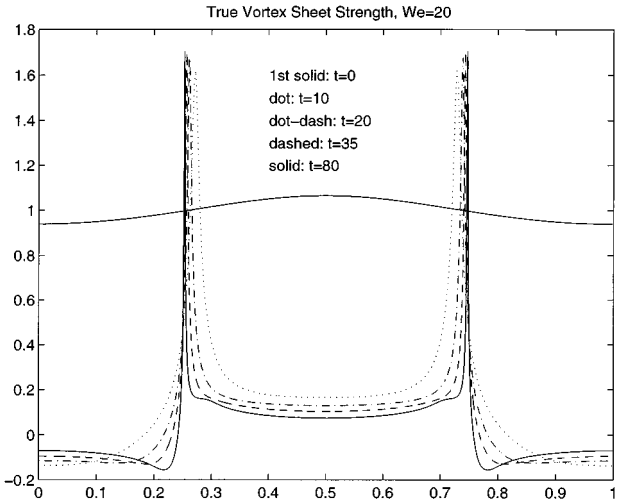

FIG. 6. $\tilde{\gamma}(\alpha,t)$ at the same times as shown in Fig. 4.

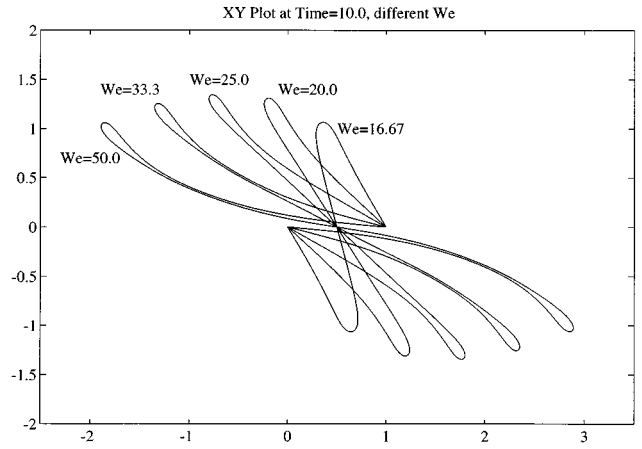

FIG. 7. The interfacial position for several values of intermediate We, at $t=10$.

of vortices upon each other. However, no such rotation is seen, and the fingers seem to lengthen more or less along a fixed angle from the x-axis.

Finally, Fig. 7 shows at $t=10$ the interfacial position for several intermediate values of We. For the largest, $We=50$, there are 4 modes initially unstable in the period. As the K–H instability becomes more important with increasing We number, the fingers become more curved by the greater relative concentration of vorticity at the origin. At values of We slightly larger than this, a sharp departure is found from the formation and smooth elongation of fingers.

As an examination of the accuracy of these simulations, the $We=50$ simulation is chosen. This simulation uses $N=1024$ and $\Delta t=10^{-3}$, up to $t=7.0$, at which point N was doubled, and Δt halved. This was to resolve the evident approach of two disparate portions of the sheet. The entire calculation, for $0\leqslant t\leqslant 10$, was repeated with a halved time-step. Assuming that time-stepping errors are dominant, then for the first simulation the maximum relative error in θ at $t=10$ is estimated to be $E_{\Delta t}\approx 1\times 10^{-4}$.

C. Large *We* and pinching

Figure 8 shows two simulations: $We=58.8$ and 62.5 (both have initially 4 unstable modes). It is between these two values of We that is seen the transition from the formation of continuously elongating fingers, to an intervening

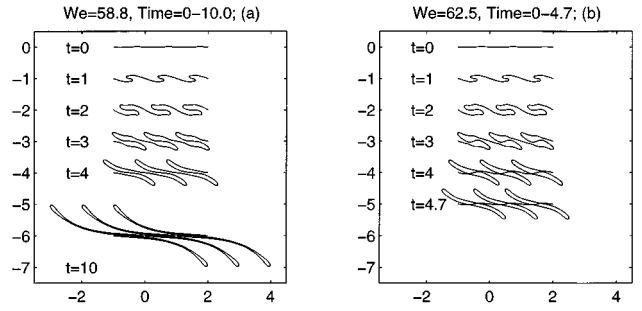

FIG. 8. The results of two simulations with $We=58.8$ (left box) and 62.5 (right box).

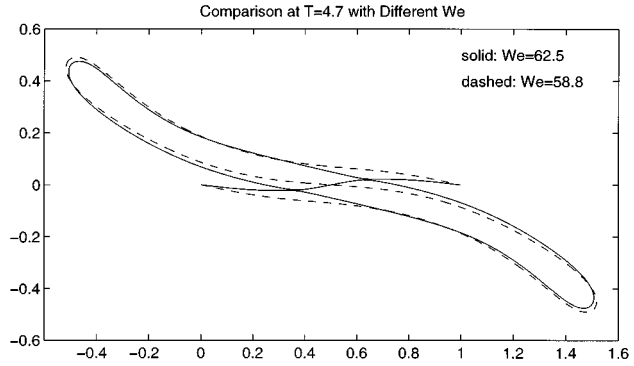

FIG. 9. The superposition of the two profiles at $t=4.7$.

event that is apparently the collision of the fluid interfaces. This collision is observed in the evolution from this initial data for every larger value of We. Figure 9 superposes the respective interface positions at $t=4.7$. Though not apparent from the scale of the figure, the colliding portions of interface for $We=62.5$ are still separated from one another by a finite distance, though this distance is diminishing rapidly. The upper two boxes of Fig. 10 shows the $\tilde{\gamma}$ at several times, for both values of We. The lowest box of the figure superposes $\tilde{\gamma}$ at $t=4.7$ for both values of We. The crucial difference is the appearance for $We=62.5$ of pairs of positive and negative spikes. These new peaks in sheet strength are situated on the colliding portions of the interface, coming in pairs, positively signed on one side, negatively on the other. This ''jet'' fluxes fluid through the narrowing neck, inflating the forming bubble.

We will not focus on the collapse process near these values of We; they are too close to the bifurcation in evolution from elongating fingers. Instead, we turn our attention to the flow for $We=200$, where the collapse occurs earlier, and the evolution is more representative of that for yet larger values of We.

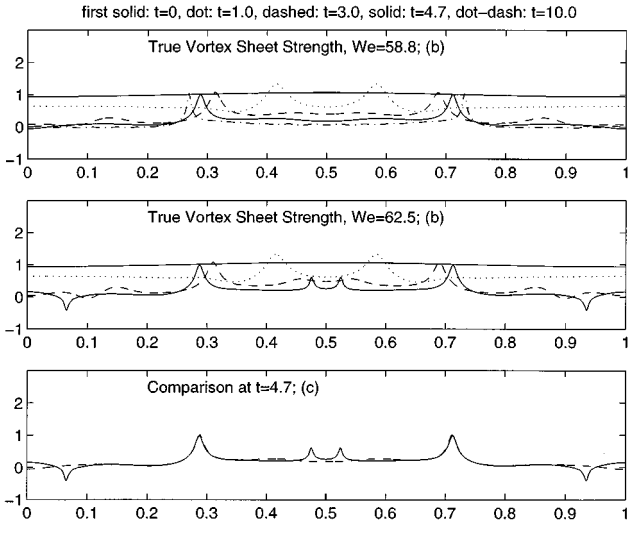

FIG. 10. $\tilde{\gamma}(\alpha,t)$ at several times (top two boxes). The lowest box superposes the vortex sheet strengths at $t=4.7$.

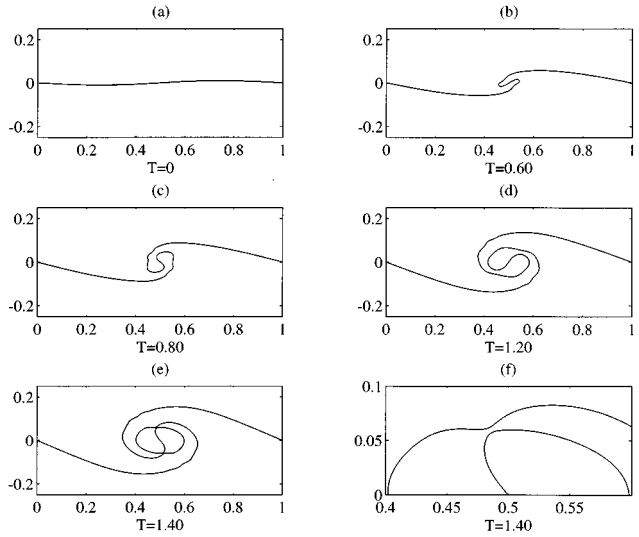

FIG. 11. The long-time evolution from a nearly flat sheet for $We=200$. The bottom right box shows a close-up of the thinning neck at $t=1.4$.

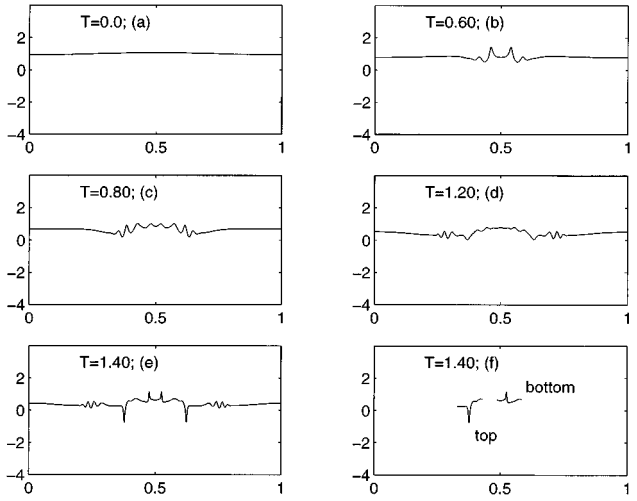

FIG. 12. $\tilde{\gamma}(\alpha,t)$ at the same times as the previous figure. The bottom right figure highlights the location of the strength extrema in the region of the thinning neck at $t=1.4$.

1. The evolution for We=200

For $We=200$, there are 16 modes initially unstable in the period, with $k=11$ the most unstable wavenumber. For $We=\infty$ the flow forms a curvature (Moore) singularity at $t_M\approx 0.37$.[19] We study first the evolution for $0\leqslant t\leqslant 1.4$ using the uniform parametrization frame. In addition, we use the implicit fourth-order time integration scheme of Ascher, Ruuth, and Wetton[35] coupled to the SSD, as described in the Appendix. The pinching singularity time is estimated to be $t_p\approx 1.427$, and the behavior for $1.4\leqslant t<t_p$ will be considered separately using both the uniform and variable parametrization frames. A time sequence of interface positions is shown in Fig. 11. This simulation uses $N=2048$ points, and a time-step of $\Delta t=1.25\cdot 10^{-4}$ on the interval $0\leqslant t\leqslant 0.36$, and $\Delta t=5\cdot 10^{-5}$ thereafter.

While at early times the interface steepens and behaves very similarly to the zero surface tension case, it passes smoothly through the Moore singularity time. At $t=0.45$, the interface becomes vertical at its center, and subsequently rolls over and produces two fingers ($t\approx 0.50$). These grow in length in the sheet-wise direction [box (b)]. The tips of the fingers broaden and roll with the sheet. This is clearly seen at $t=0.80$ [box (c)], as are evident capillary waves, seen as oscillations along the sheet. These waves are approximately on the scale of the most unstable wavelength given by the linear analysis. By $t=1.20$ [box (d)], the sheet produces another turn in the spiral, and the fingers become broader and larger. Additional capillary waves are produced and traverse the interface outwards from the center region. This dispersive effect of the surface tension is seen more clearly in plots of the curvature and vortex sheet strength. Note that the part of the interface (on the inner turn) closest to the fingers has become quite flat and bends very slightly towards the fingers. At later times, this part bends even more towards the fingers, the tips of the fingers narrow, and both pieces of the interface approach each other. At $t=1.40$ [box (e)], the interface appears to self-intersect, but a close-up of the region at this time [box (f)] indicates there is still a finite distance between the upper finger and the inner roll. The same is true for the lower finger by symmetry, although that symmetry is not explicitly imposed in the simulation.

At this time, the gap between the two approaching portions of interface is but 5 grid lengths wide, and the calculation is stopped here. As shown in Baker and Shelley[38] accuracy is rapidly lost in trapezoidal quadratures of the Birkhoff–Rott integral as the distance between the interfaces falls below a few mesh spaces. By this time, the length of the interface has increased by a factor of 2.6 .

Figure 12 shows the vortex sheet strength $\tilde{\gamma}$, vs α. It is worth recalling here a few properties of the Moore singularity for $We=\infty$. As the singularity time is approached, the maximum in $\tilde{\gamma}$ sharpens to form a finite cusp at $\alpha=1/2$. In the same approach, the curvature κ diverges positively at $\alpha=1/2^-$, and negatively at $\alpha=1/2^+$. And so as κ diverges, κ_α diverges negatively at $\alpha=1/2$. In the presence of a small surface tension [using Eq. (10)], this behavior will cause $\tilde{\gamma}_t$ to be negative at the peak, thereby reducing and eventually fissioning the maximum in $\tilde{\gamma}$ (see also Ref. 33).

This effect, explained heuristically above, likely explains the appearance of the two dominant, positive peaks seen in $\tilde{\gamma}$ at $t=0.6$. Small waves have also formed at the outer edges of these peaks, and are presumably dispersive waves produced by the surface tension saturation of the Moore singularity. At $t=0.80$ [box (c)], the peaks have saturated and more waves have been produced. These disperse outward along the interface. The strength $\tilde{\gamma}$ has also formed downward peaks at the edge of the wave packet. The saturation and dispersion continues through $t=1.20$ [box (d)]. However, when the interface begins to self-approach, the vortex sheet strength refocuses, forming a jet. This jet is seen at $t=1.40$ [box (e)] in the pairs of positive and negative peaks of vortex sheet strength that have formed in each pinching region. These peaks have been isolated for the top pinching *region* in box (f). The top of the pinching region (inner turn

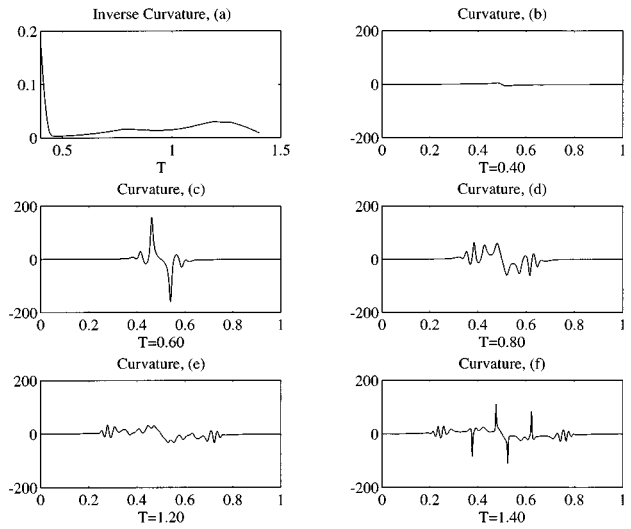

FIG. 13. The curvature. The upper left box shows the evolution of the inverse curvature. The remaining boxes show the curvature of the interface at the same times as the previous figure.

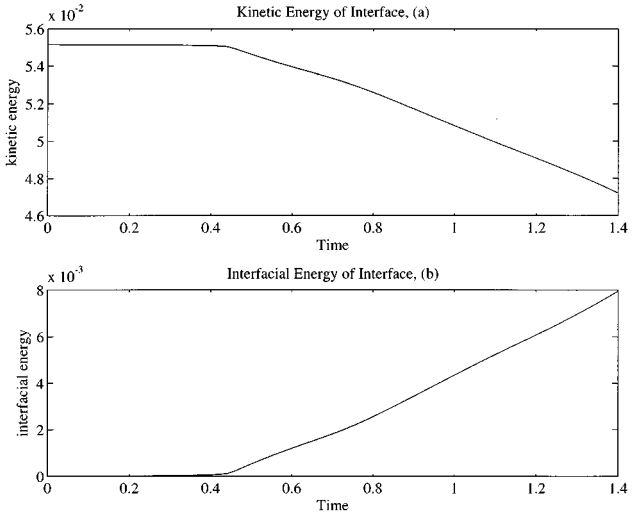

FIG. 14. The decomposition of the total energy into the perturbation kinetic energy (upper box), and the interfacial energy (lower box).

of the spiral) comes with a negative signed vortex sheet strength and the bottom comes with a positive sign. This implies fluid is streaming through the gap towards the center and into the downwardly pointing finger. For this initial data (single-signed sheet strength), such a sign change in the vortex sheet strength can occur *only* in the presence of surface tension.

Saturation and refocusing are also observed in the curvature. Its evolution is plotted in Fig. 13. The first graph shows the inverse maximum of the absolute curvature as a function of time. There is an initial region of rapid growth in the curvature (decay in the plot) due to the Moore singularity. But, the curvature growth saturates and its spatial peaks break up into dispersive waves [boxes (d) and (e)] moving outwards from the center. By $t=1.40$, the maximum of the curvature nearly reaches that attained during the initial period of growth, and the new refocusing and growth occurs at the points of nascent pinching. These points are associated with pairs of like-signed peaks in the curvature.

Figure 14 shows the decomposition of the total energy into the perturbation kinetic energy (upper box), and the interfacial energy (lower box). The beginning of roll-up is plainly seen by the transfer of energy into the interfacial energy. This occurs soon after the Moore singularity time. Nothing is seen in this figure that indicates the oncoming collision of interfaces, except perhaps a slight increase in slope for the interfacial energy.

There are two events which cause losses of accuracy in the time integration. The first is the shadow of the Moore singularity. At times less than $t_M=0.37$, there are nearly 14 digits of accuracy in the energy. At times slightly beyond t_M, the number of accurate digits in the energy drops to 11 where it remains until the sheet approaches self-intersection. In this second loss, near $t=1.4$, a number of accurate digits in the energy drops to 10. As is typical, estimates of the point-wise relative error (discussed below) are larger than those of the energy. Comparison with simulations with lower spatial resolution suggest that temporal errors are dominant, and the error of this simulation was again checked by halving the time-step. The estimated relative error in θ is found to be approximately 1×10^{-7} at $t=1.2$, and 4.5×10^{-7} at $t=1.4$. We found that use of the fourth-order time-integration improved our accuracy by 3 to 4 digits over the second-order Crank–Nicholson method for the same time-step (see HLS94).

2. Near the singularity time

Maintaining numerical resolution is critical as the singularity time is approached. There are several possible sources of error. First, the thickness of the collapsing neck decreases to zero with infinite slope (close to a 2/3 power in time), and as this distance decreases, $\tilde{\gamma}$ and the curvature κ both diverge. Time-steps must be taken small enough to resolve these trends. Spatial resolution must also be sufficiently high in the regions of close approach to resolve both the spatially diverging $\tilde{\gamma}$ and κ, and to evaluate accurately the contribution of the collapsing neck region to the Birkhoff–Rott integral.

Due to their relative efficiency, the uniform parametrization simulations are pushed as closely as is practical towards the collapse time. This is accomplished by using successive doublings of the spatial points N, and halvings of Δt. The doubling is done by Fourier interpolation, at times when the thickness of the collapsing neck is still approximately 10 grid lengths wide, for which the trapezoidal sum is still very accurate.[38] For $N=2048$ this time is $t=1.34$. Examination of the spatial Fourier spectrum at this time shows also that the active part of the spectrum is well away from the Nyquist frequency $k=N/2$. The table below tabulates resolutions and intervals for the various runs. By increasing the spatial resolution, 11 digits of accuracy in the energy can be maintained until $t=1.39$ for $N=2048$, $t=1.41$ for $N=4096$, and $t=1.42$ for $N=2048$.

The variable parametrization runs are all begun at $t=1.413$ (this choice of time is again made by the same

TABLE I. The two tables show, with associated time intervals, the spatial and temporal resolutions of both the uniform and variable parametrization simulations.

Uniform parametrization			Variable parametrization		
N	Δt		N	Δt	
2048	1.25×10^{-4}	$0\leqslant t\leqslant 0.36$	2048	5×10^{-6}	$1.413\leqslant t\leqslant 1.427$
	5×10^{-5}	$0.36\leqslant t\leqslant 1.4$	4096	2.5×10^{-6}	$1.413\leqslant t\leqslant 1.427$
4096	2.5×10^{-5}	$1.34\leqslant t\leqslant 1.427$	8192	1.25×10^{-6}	$1.413\leqslant t\leqslant 1.427$
8192	1.25×10^{-5}	$1.39\leqslant t\leqslant 1.427$			

rule— the neck width is at least 10 grid lengths) from the $N=8192$ uniform parametrization data. Again the initial data is generated by Fourier interpolation. The mapping which generates the parametrization of the curve is described in Appendix A. It clusters points locally about the collapse regions; the parameters of this remapping are chosen so that the local resolution is 8 times greater than for the uniform parametrization with the same value of N. The mapping is completely fixed during the calculation by the choice of tangential velocity T in Eq. (33). Again, the Table I shows the values of N and Δt. A resolution study near the singularity time will be presented later in this section.

The top graph of Fig. 15 shows the minimum width of the neck in the upper pinching region. The medium dashed curve is the width measured from the $N=8192$ uniform parametrization simulation, while the solid is that from the variable parametrization simulation (also for $N=8192$). This minimum width is computed by minimizing the distance function between the opposing sections of the interface, constructed using the Fourier interpolant of the curve position. The trend of the least distance towards zero is clear. While it is not clear here, it will be seen later that the variable parametrization simulations do give better results near the singularity time.

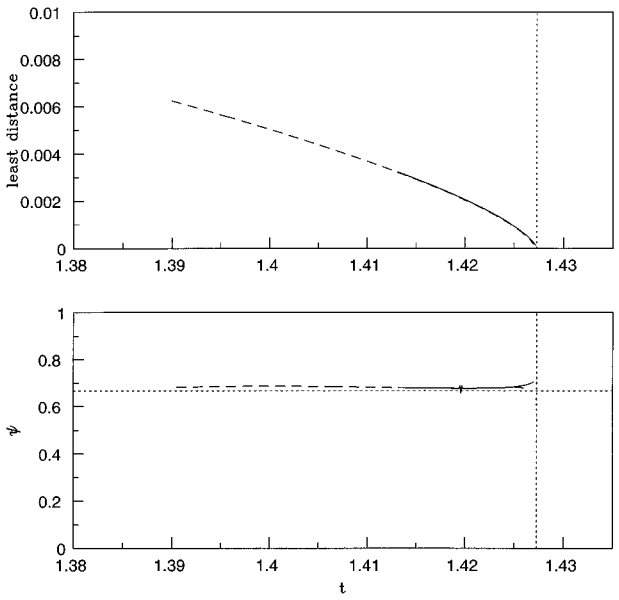

FIG. 15. The upper box shows the minimum width of the neck in the upper pinching region. The lower box shows the exponent in an algebraic fit to the minimum width. The vertical dashed line in both boxes marks the fit to the singularity time. The horizontal dashed line is at 2/3.

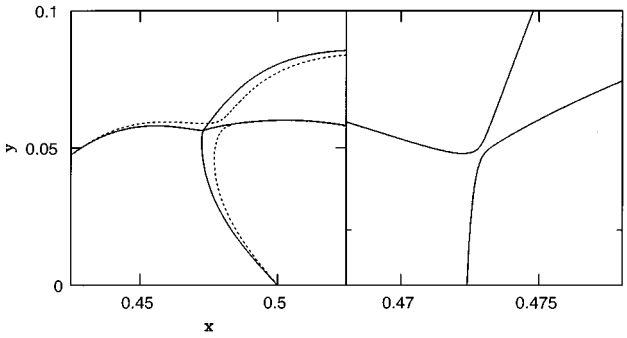

FIG. 16. The left box shows a close-up of the top pinching region of the rolled-up sheet at times $t=1.4135$ (dashed) and 1.427 (solid), both very near the collapse time. The right box magnifies this close-up by another factor of 10.

An algebraic fit of the form

$$\textit{Least Distance}=d(t)=A(t_p-t)^{\psi_d}, \tag{35}$$

is made to the neck width. This is done as a sliding fit to successive triples of data $[(t_i,d(t_i)),i=1,2,3]$ to determine the three unknowns A, t_p, and ψ_d. The fits to ψ_d are shown in the lower graph of the figure. While the fits are not completely flat, particularly very near the singularity time, they are generally close to 2/3 (shown as the horizontal dashed curve). Recall that $\psi_d=2/3$ is the temporal exponent obtained through similarity considerations. The fit to the collapse time t_p was given consistently as $t_p=1.4273\pm.0002$. This is shown as the vertical dashed line in both graphs of the figure.

While the collapse of the neck width must be (and is) accompanied by the divergence of velocity gradients in the fluid, as demonstrated in Appendix C, it is also accompanied by loss of smoothness in geometric quantities of the sheet, notably its curvature. The left graph of Fig. 16 shows a close-up of the top pinching region of the rolled-up sheet at times $t=1.4135$ (dashed) and 1.427 (solid), both very near to the collapse time. The right graph magnifies this close-up by another factor of 10 to show that the neck at the later time has not yet collapsed. It appears that the sheet is forming two opposing corners on either side of the neck. This is in agreement with the upper graph in Fig. 17, which shows the tangent angle θ, as a function of normalized arclength (this would be α in the uniform parametrization frame). Arrows indicate two of the four locations along the θ curve where the curvature, $\kappa=\theta_s$, is diverging. These sections are shown as close-ups in the lower graph of the figure, again at times $t=1.4135$ (dashed) and $t=1.427$ (solid). It appears from these (most especially in the left graph) that θ is sharpening to a jump discontinuity with the collapse, indicating the formation of a corner in the sheet profile. It does not appear from these figures that the two angles are equal. The curvature itself is shown in the top graph of Fig. 18, at both of these times.

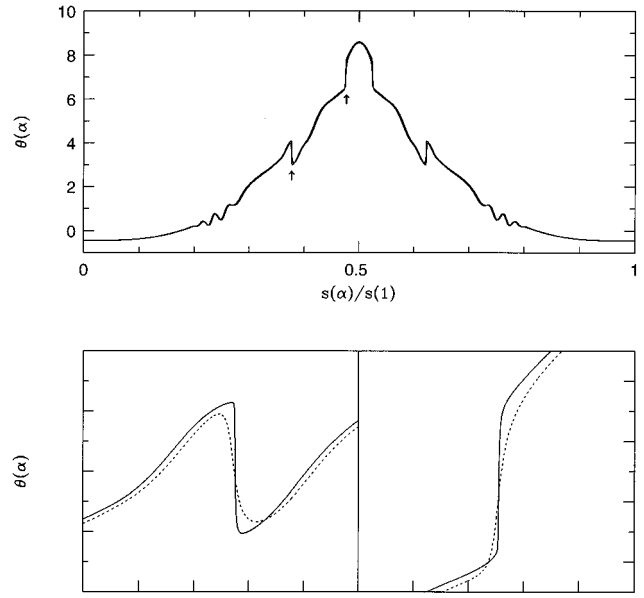

FIG. 17. The upper box shows θ as a function of normalized arclength. The lower boxes show close-ups of the regions indicated by arrows in the upper box, at $t=1.4135$ (dashed) and 1.427 (solid).

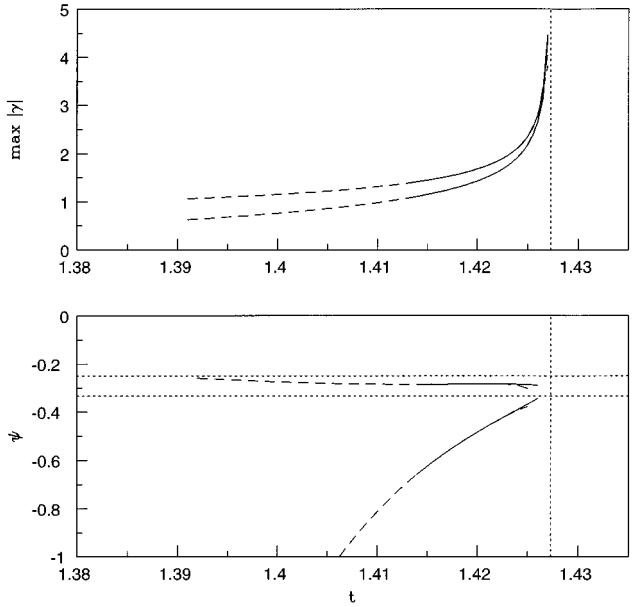

FIG. 19. The upper shows the time evolution of the two extremal true vortex sheet strengths. The lower box shows the fit to ψ_γ for these two extrema. The horizontal dashed lines are at $-1/4$ and $-1/3$. The vertical dashed line is a fit to the singularity time.

The lower graph of the figure shows $\tilde{\gamma}$ at these times. Its apparent divergence fulfills the requirement that at least velocity gradients diverge as a collapse is approached.

If the collapse is governed by similarity, as might be indicated by the fits to ψ_d for the neck width, then the predicted similarity exponents are $\psi_\kappa=-2/3$ for curvature, and $\psi_\gamma=-1/3$ for the vortex sheet strength. This scenario is now complicated by the fact that there are two values of $\tilde{\gamma}$, and of κ, to be considered, one on either side of the collapsing neck. The upper box of Fig. 19 shows the growth of these two extremal vortex sheet strengths, again for the $N=8192$ uniform (dashed) and variable (solid) parametrizations. The branching near the singularity time in these mostly overlapping fits is caused by a loss of accuracy in the uniform parametrization simulation.

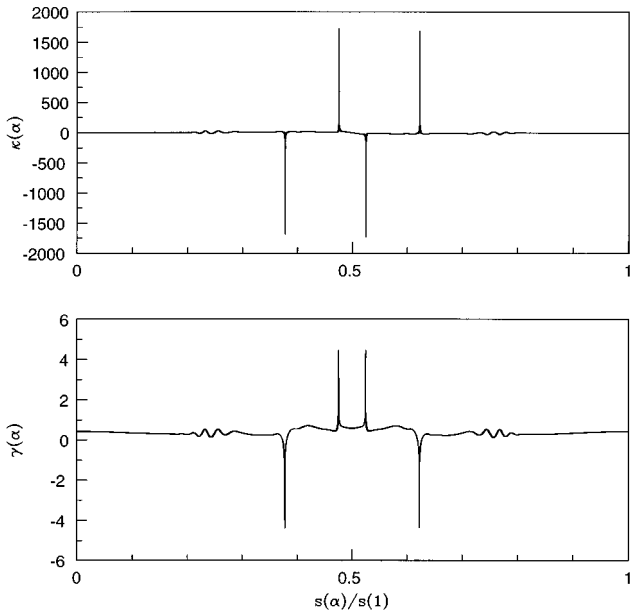

FIG. 18. The top box shows the curvature at the same times as in the previous figure. The lower box shows true vortex sheet strength.

The lesser of the two curves is the negative extremum of $\tilde{\gamma}$ on the upper side of the neck, and the other curve the positive extremum on the lower side. They both appear to be diverging. The lower box of the figure shows the fit to ψ_γ for these two extrema. The lower curve is again that for the negative extremum. The dashed curves are at $\psi_\gamma=-1/3$ and $-1/4$. The fit for ψ_γ for the positive extremum is fairly flat, lying somewhere between these two values. On the other hand, the assumption of a uniform value for ψ_γ of the negative extremum is plainly inappropriate, though the two values of ψ_γ might be converging to each other as the critical time is approached. At any rate, an argument for precise similarity scaling is not much strengthened by these fits.

We did attempt to refine the fit by using a higher-order Ansatz (adding another algebraic term) but found that attaining convergence of Newton's method was difficult. No better agreement with similarity was found by using the value of $\tilde{\gamma}$ at the point of least separation distance, rather than the maximum value of $\tilde{\gamma}$.

Similar fits for the extremal curvatures are shown in Fig. 20. The respective signs of the curvatures match those of $\tilde{\gamma}$, and again, the lower curve in the upper graph is that of the negative curvature on the upper side of the neck. Now the appropriateness of the algebraic fit is suspect in either case, though the two fits seem to be approaching each other in value (but not to $-2/3$) as the critical time is approached. Here, the two horizontal dashed lines are $\psi_\kappa=-2/3$, the putative similarity exponent, and $\psi_\kappa=-1/2$. Again, the

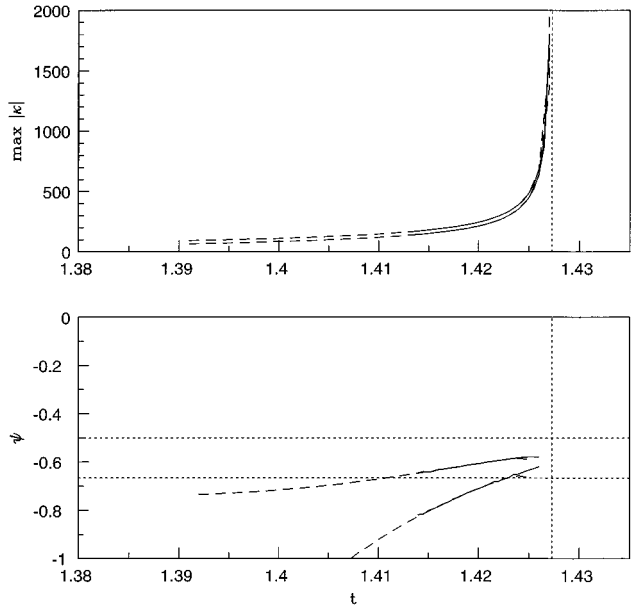

FIG. 20. The upper shows the time evolution of the two extremal curvatures. The lower box shows the fit to ψ_κ for these two extrema. The horizontal dashed lines are at $-1/2$ and $-2/3$. The vertical dashed line is a fit to the singularity time.

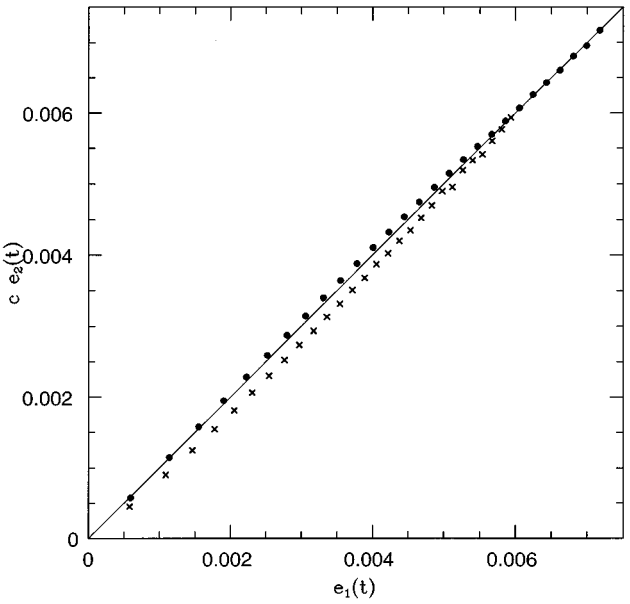

FIG. 21. $\epsilon_1(t)$ versus $c\cdot\epsilon_2(t)$ calculated on both sides of the neck (upper side as dots, lower side as crosses), where c is a constant of proportionality determined from the first data point (in the upper right corner).

branching near the singularity time is due to loss of accuracy in the uniform parametrization simulation.

While the divergence of κ does not apparently conform to similarity, there is some evidence for a local scaling behavior consistent with forming a corner singularity. Suppose that κ behaves locally in the neck region as

$$\kappa(s,t)\sim\frac{1}{\epsilon_1(t)}K\left(\frac{s-s_p(t)}{\epsilon_2(t)}\right), \tag{36}$$

where $\epsilon_{1,2}\to 0$ as $t\to t_p$, and s_p locates an extremum of κ. Then, $\epsilon_1(t)\propto\epsilon_2(t)$ corresponds to θ forming a jump discontinuity at $(t,s)=(t_p,s_p(t_p))$. We set ϵ_1 to $1/|\kappa(s_p,t)|$, and estimate ϵ_2 by $|\kappa(s_p,t)/\kappa_{ss}(s_p,t)|^{1/2}$. Figure 21 shows $\epsilon_1(t)$ versus $c\cdot\epsilon_2(t)$ calculated on both sides of the neck (dots are the upper side, crosses the lower side), where c is a constant of proportionality determined from the first data point in the upper right corner. It is especially for the upper side of the neck that ϵ_1 and ϵ_2 appear to be linearly related.

We have also tried to find local scaling behavior in the divergence of $\tilde{\gamma}$ by using a scaling Ansatz as in Eq. (36). The similarity exponents for $\tilde{\gamma}$ suggest then that $\epsilon_2\propto\epsilon_1^2$. While we did find collapsing scales $\epsilon_{1,2}$ accompanying the $\tilde{\gamma}$ divergence, it was not found that ϵ_1 and ϵ_2 were related in this way.

Such well-resolved, variable parametrization calculations have also been performed for the $We=100$ case but are not presented here. The results are basically consistent with those for 200: only a partial conformance with similarity behavior, but the apparent formation of a corner singularity in the sheet profile. The apparent limiting exponents, such as suggested by Fig. 20, were yet further from the similarity exponents.

While our results do not suggest strict conformance with similarity behavior, we must emphasize the usual caveats when dealing with the numerical analysis of numerical data. It is quite possible that similarity does govern the oncoming singularity, but that we have not yet been able to reach, with sufficient accuracy, the regime governed by similarity. Further, perhaps our results would show better agreement with similarity by using other data fitting tools that stably account for corrections from higher-order behavior.

3. An analysis of numerical errors near $t=t_p$

For the case of $We=200$, we give a discussion of the accuracy of our numerical simulations near the singularity time, focusing on quantities especially relevant to the singularity development. As an initial measure of the error, we note that while the energy is generally very well conserved, the uniform mesh calculations lose accuracy rapidly as the singularity time is approached. Since extra filtering is required to control the stronger aliasing instabilities associated with the variable mesh, this results generally in less accuracy in the variable mesh simulations, relative to the uniform parametrization simulations, at times away from the singularity time. For example, at time $t=1.415$, there are 8 accurate digits in the energy for the variable mesh calculations (compared to 11 for the uniform mesh with $N=8192$). However, in the variable mesh simulations, there is almost no degradation in the number of accurate digits in the energy near the singularity time.

A stronger test is to look for consistency with convergence in some pointwise quantity. First, consider $d(t)$, the collapsing least distance of the neck region, with the $N=8192$ variable parametrization simulation serving as the ''exact'' solution. Figure 22 shows the number of significant digits of agreement in $d(t)$ of the reference simulation with

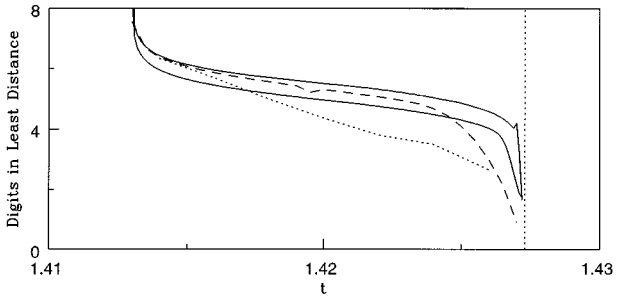

FIG. 22. The number of significant digits of agreement in $d(t)$ with the highest resolution simulations.

the other simulations, as estimated by $-\log_{10}|d_r(t) - d(t)|/|d_r(t)|$ where d_r is the reference solution. Consistency with convergence is evident. The two solid curves are for the $N=2048$ and 4096 variable parametrization simulations. The latter lies above the former, and is thus presumably more accurate. As before, the dashed curves are for the $N=4096$ (short dash) and 8192 (long dash) uniform parametrization simulations, with the more resolved calculation showing more agreement with the reference solution, and again losing accuracy as the singularity time is approached. This study does not measure the accuracy in the reference simulation, and the $N=8192$ variable parametrization simulation presumably has yet higher accuracy.

The upper box of Fig. 23 shows at $t=1.427$ a blow-up of a curvature spike (see Fig. 18) in the thinning neck region, as computed by both the $N=8192$ uniform and variable resolution simulations. The crosses mark the computational mesh points. The differences in resolution of the spike are obvious. Within this region the variable mesh has about 8 times more

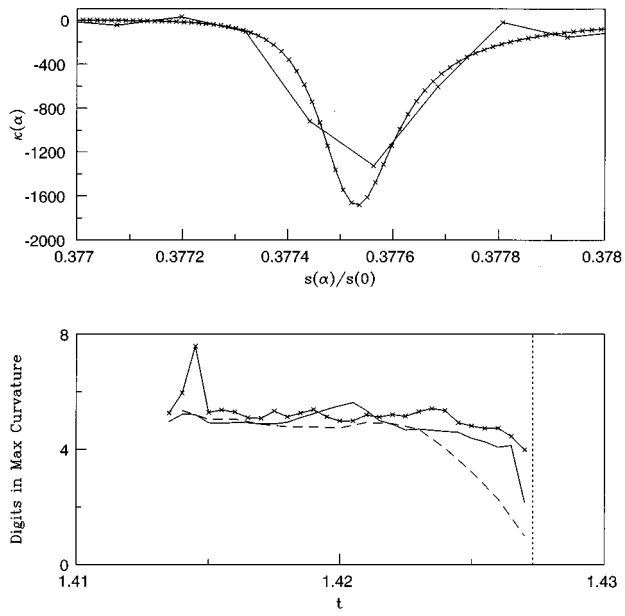

FIG. 23. A blow-up of a curvature spike in the thinning neck region, as computed by both the $N=8192$ uniform and nonuniform resolution simulations, at $t=1.427$. The crosses mark the computational mesh points. The lower graph shows the number of significant digits of agreement in the maximum curvature with the highest resolution simulations.

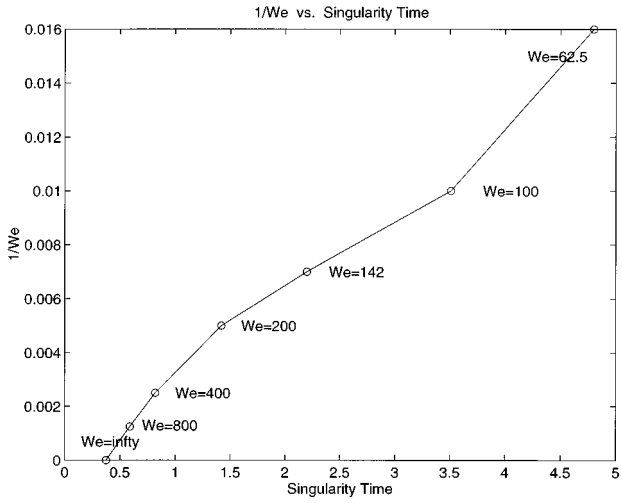

FIG. 24. The pinching singularity time as a function of decreasing We^{-1}, with the Moore singularity time included at $We^{-1}=0$.

points than the uniform mesh, and does not suffer from the oscillations of the uniform parametrization calculation. To analyze the accuracy in the curvature quantitatively, the convergence of the maximum curvature κ_{max} is examined as a function of the spatial resolution, just as was done above for the least distance $d(t)$. Again, the $N=8192$ variable parametrization computation serves as the reference simulation. The lower box of Fig. 23 shows the number of significant digits of agreement in κ_{max} of the reference simulation with the other simulations. The curve marked with crosses is the variable parametrization calculation with $N=4096$, the solid curve is the variable parametrization calculation with $N=2048$ and the dashed curve is the uniform parametrization calculation with $N=8192$. Consistency with convergence is again evident and the results are quite similar to those obtained for the least distance $d(t)$ in Figure 22.

4. Relations to the Moore singularity

In previous studies on the effects of regularization on the Moore singularity — using δ-smoothing,[39] contour-dynamics,[40] or by adding viscosity[41,42] — it was generally observed that a spiral structure would emerge in the flow. As the regularization parameter was taken to zero, this spiral would acquire more and more structure, and its time of emergence would decrease towards the Moore singularity time. It is known that these regularized flows exist and are smooth for all time.[43–45] With small surface tension, the emergence of a spiral is again observed, but now the smooth evolution of the flow is abbreviated by the appearance of the pinching singularity.

An upper bound on the time at which the spiral emerges in the surface tension case is the time at which the pinching singularity occurs. Figure 24 shows the pinching singularity time as a function of We^{-1}, with the Moore singularity time included. It does appear that the Moore singularity time is the limit of the pinching times and thus the time of emergence of the spiral also decreases to the Moore singularity time. The largest Weber number used for this initial data is $We=800$. Figure 25 shows sheet profiles over several dou-

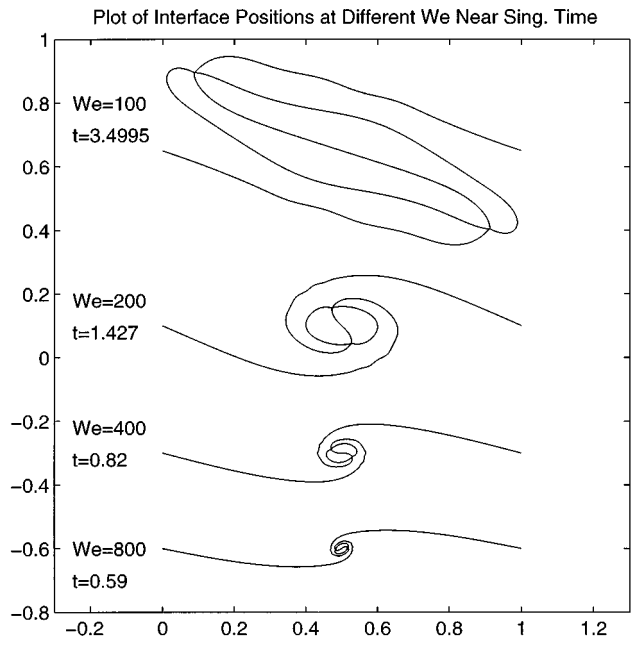

FIG. 25. The sheet profiles, over several doublings of We, at times close to their pinching singularity times.

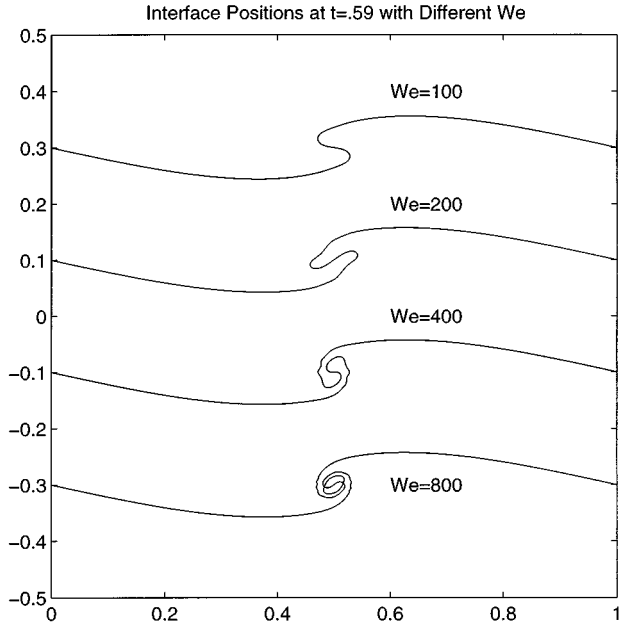

FIG. 27. The interface positions for the various Weber numbers, at $t=0.59$, approximately the pinching time for $We=800$.

blings of We, at times close to their pinching singularity times. As We is increased, the pinching occurs earlier, and the spiral becomes smaller, but it does not turn a great deal further, or acquire much more structure. The dispersive effect of surface tension is seen in the packet of small amplitude waves spreading out from the spiral region. As discussed earlier, this packet is associated with the shadow of the Moore singularity.

Figure 26 shows $\tilde{\gamma}$ at these times, likewise revealing a complicated structure. In the center region are the peaks of positive and negative sheet strength associated with the jets in the neck regions. This is separated from a smooth region, outside of the spiral, by the travelling wave packet. This wave packet might be termed a dispersive ''internal layer.'' As We is increased, this packet becomes both narrower and of higher frequency — its wavelength decreases linearly (very approximately) with We^{-1}. It is not clear whether its amplitude also generally increases. At $t=0.59$, approximately the pinching time for $We=800$, Fig. 27 shows the interface positions for the various Weber numbers, and Fig. 28 shows $\tilde{\gamma}$.

A simple spatial and temporal rescaling seems to collapse some of the sheet behavior immediately after the Moore singularity time. In particular, we have attempted to describe the length and time scales of the ''tongue'' of fluid that initially emerges in the center (see the top box of Fig. 30). Consider the rescaled time,

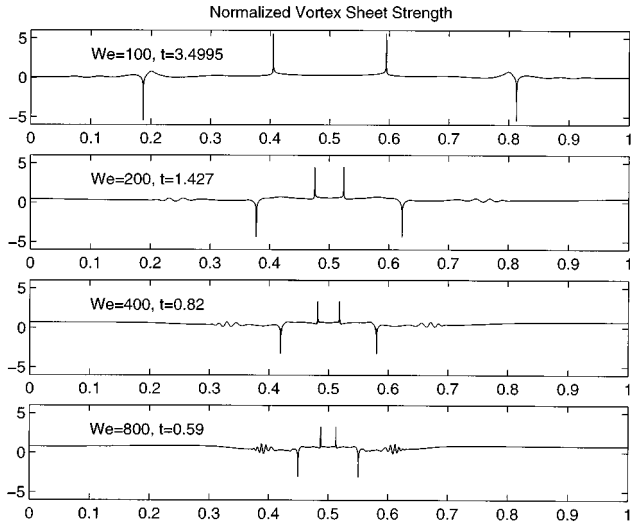

FIG. 26. $\tilde{\gamma}$ at the same times as the previous figure.

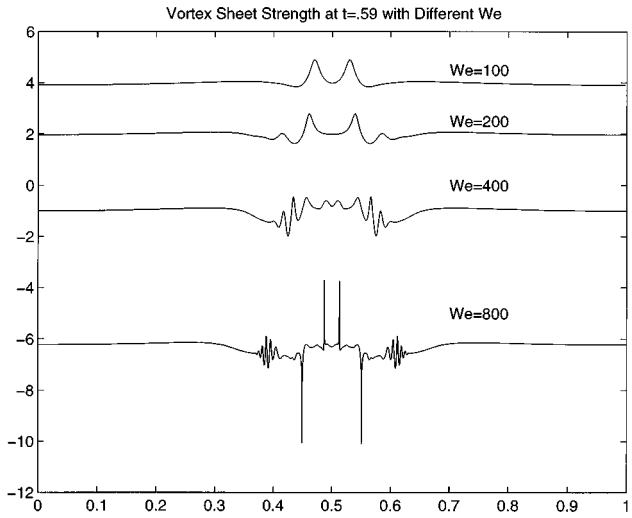

FIG. 28. $\tilde{\gamma}$ for the various Weber numbers, at $t=0.59$.

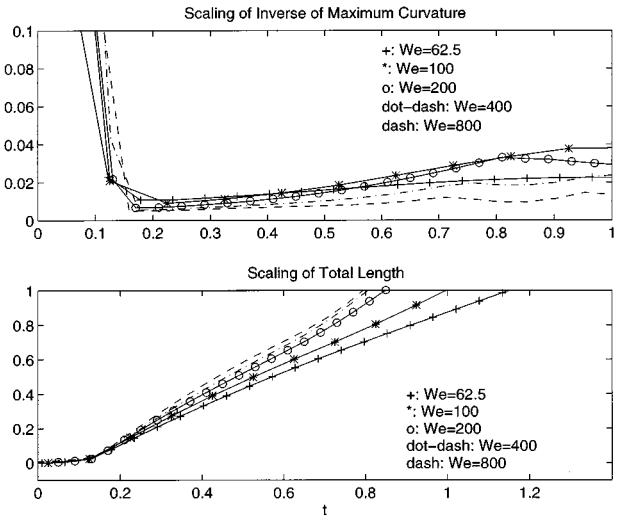

FIG. 29. Rescaled lengths and widths of the interface ''tongue,'' for several values of We, soon after the Moore singularity time.

$$t' = \frac{We}{We_0}(t - t_M),$$

where $We_0 = 100$ is used as a reference value, and t_M is the Moore singularity time. Using this rescaled time, the top box of Fig. 29 shows the rescaled width,

$$w_{We}(t') = \frac{We}{We_0}\frac{1}{\overline{\kappa}(t')},$$

where $\overline{\kappa}$ is the maximum absolute curvature of the sheet. This extremum occurs at the tip of the tongue, and so w_{We} is a measure of the tongue width. The bottom box of Fig. 29 shows the rescaled curve length,

$$l_{We}(t') = \frac{We}{We_0}(L(t') - L_0),$$

where L_0 is the length of the vortex sheet, with no surface tension, at the Moore singularity time. The quantity l_{We} is then a measure of the length of the tongue. These two length-scales seem well-described by this rescaling, at least for times soon after the Moore singularity. The top box of Fig. 30 shows the sheet position, for the three largest Weber numbers, near the rescaled time $t' = 0.3$. The lower box shows the superposition of the three center tongues after the spatial rescaling by We/We_0 as suggested above ($We = 200$ solid, $We = 400$ dash–dotted, $We = 800$ dashed). The three tongues lie nearly on top of each other.

As is clear from Fig. 29, these rescalings do not appear to describe behavior up to the pinching time. However, the results do suggest that some aspects of the flow might be described by the emergence of simple, self-similar structures — here the tongues — soon after the Moore singularity time. A self-similar structure has been conjectured to describe the spirals that emerge in the δ-smoothing regularization of the Kelvin–Helmholtz problem.[39]

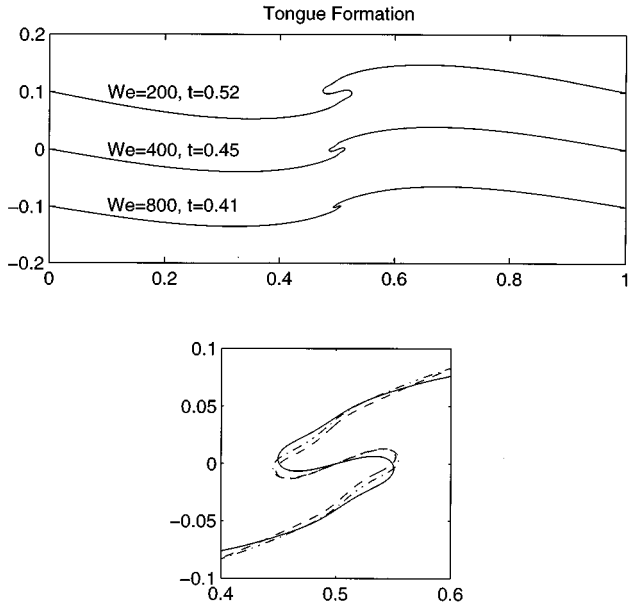

FIG. 30. Sheet position for the three largest Weber numbers, at times near $t' = 0.30$. The bottom box superposes the three center tongues after spatial rescaling by We ($We = 200$ solid, $We = 400$ dash–dotted, $We = 800$ dashed).

D. Simulations from more general data

Finally, we have performed simulations of yet more complicated initial data for a single sheet. The upper box of Fig. 31 shows two periods of the evolution, with $We = 200$, from a nearly flat sheet. The initial data lies in the $k = 1$ and 3 modes, with randomly chosen phases. As $k = 3$ is the more unstable mode, the dominant structures appear at that scale, but with considerable asymmetry introduced by the subharmonic part of the perturbation. Again, the evolution is apparently terminated by the appearance of a pinching singularity in the rightmost spiral. The lower boxes shows evolution

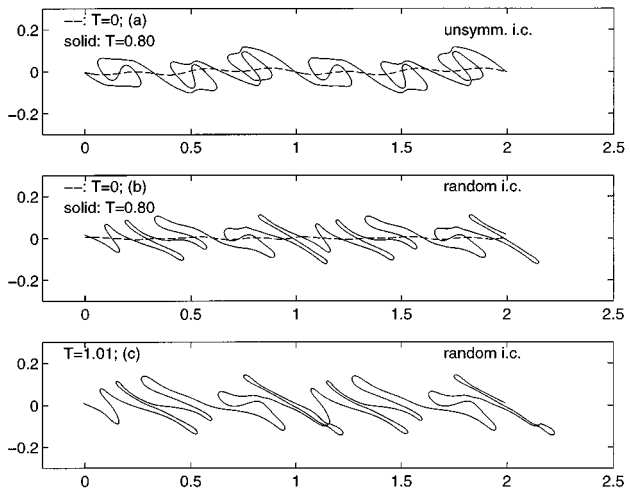

FIG. 31. The development of the Kelvin–Helmholtz instability, with $We = 200$, over two periods from nonsymmetric initial data. (a) The initial data is in the $k = 1$ and 3 modes, each with a randomly chosen phase. (b) and **(c)** The initial data is in the first 30 modes, with randomly chosen initial amplitudes and phases.

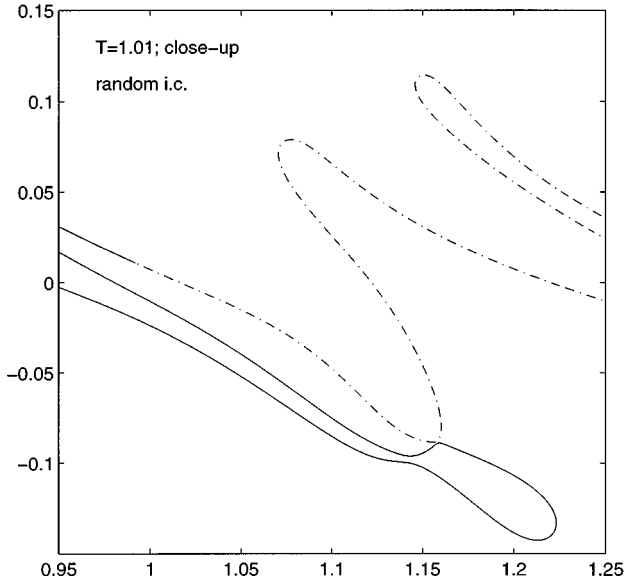

FIG. 32. A blow-up of the pinching singularity in (c) of the previous figure.

from an even more complicated initial condition, again for $We=200$. Here the first 30 modes have randomly chosen amplitudes and phases. The amplitude as a function of k is cut off exponentially, so that the $k=30$ amplitude lies below the order of the round-off (10^{-14}). Now, one sees an even greater variety of structures — both growing fingers and rolled up regions. It appears that the whole structure is somewhat stabilized *against* pinching by the fingers, which stretch the interface. Nonetheless, the evolution is again terminated by a pinching singularity, this time along the side of a downwardly propagating finger. The pinching occurs between this finger and the leftmost downward finger in the periodic extension of the interface. This is most clearly seen in Fig. 32 which shows a close-up of the interface profile. The solid and dash-dotted curves show the interface and its periodic extension, respectively.

V. DISCUSSION AND CONCLUSION

The precise mechanisms that might link the Moore singularity to the pinching singularity are unclear. However, the pinching does seem to follow from the concatenation of several physical processes. The first is the Kelvin–Helmholtz instability, which concentrates circulation at points along the vortex sheet. As this concentration intensifies, the dispersion from surface tension becomes important, and both ''splits'' the peak in $\tilde{\gamma}$ and creates oscillations (see Fig. 26). Simultaneously, due to the bulk concentration of circulation, the sheet begins to roll up into a spiral. The spiral structure allows the oscillations along disparate sections of the sheet to strongly interact and couple, ultimately creating oppositely signed circulation on either side of a now thinning neck. This interaction and ensuing neck formation we do not understand well.

With the formation of the jet, the neck collapses rapidly. This motivates us to examine the dynamics of isolated jets between two interfaces. To make the situation as simple as possible, consider first two vortex sheets (1 and 2) under surface tension, with initial conditions satisfying

$$x_1=x_2, y_1=-y_2, \text{ and } \gamma_1=-\gamma_2.$$

This up/down symmetry is preserved by the subsequent evolution. The upper box of Fig. 33 shows the simulations of the collapse of such a jet, with the data chosen so that there is only one linearly unstable mode in the period. Clearly, the pinching singularity occurs directly in this setting, without the additional feature of the roll-up into a spiral. Figure 34 shows evolution from the same initial data (dashed), but with $We=\infty$. The final time shown (solid) is that very near the formation of a Moore singularity, appearing simultaneously on the upper and lower sheets. The solid dots mark the location on the sheets of the emerging singularity. It seems evident that the beginnings of the collapse are seen in the dynamics of a jet without surface tension. Perhaps a

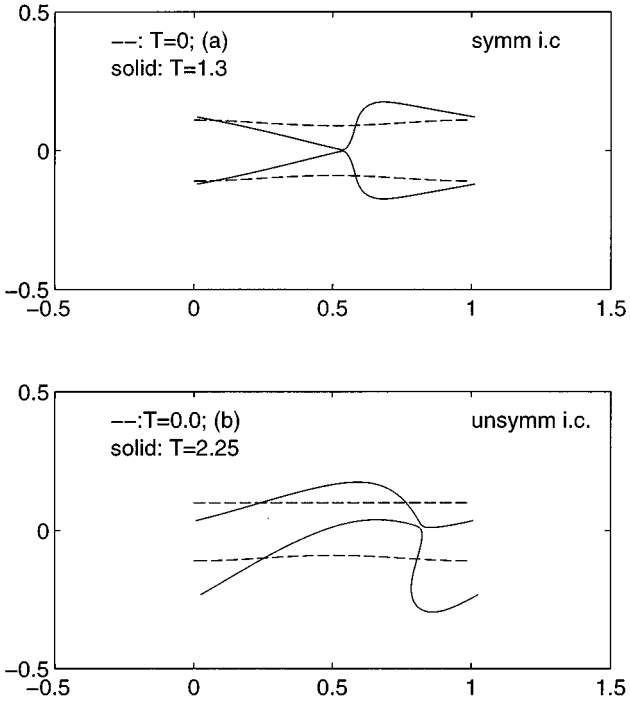

FIG. 33. (a) The formation of a pinching singularity in a symmetric jet between two interfaces with surface tension. (b) The same as (a) but the upper interface has zero initial circulation and is flat.

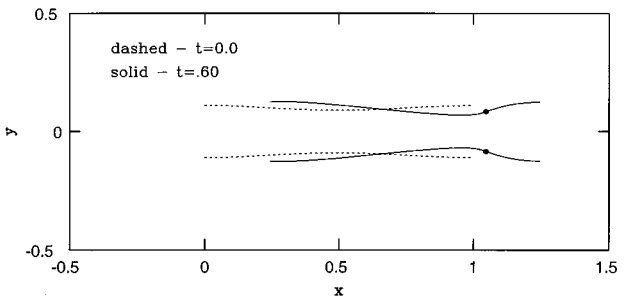

FIG. 34. The formation of the Moore singularity in a symmetric jet between two interfaces without surface tension. The solid dots mark the location of diverging curvature.

''secondary'' Kelvin–Helmholtz instability is intimately related to the formation of the pinching singularity. In this direction, Pugh and Shelley[46] have been studying asymptotic models of such jets with surface tension.

The lower box of Fig. 33 shows a much different simulation. The lower interface has the same initial data as in the previous simulation, but the upper interface now begins with zero vortex sheet strength, and is flat. Therefore, at early times the upper interface behaves as a curve material to the flow. The lower interface is unstable to the K–H instability, and its amplitude grows. This growth perturbs the upper interface, and appreciable circulation is produced. The two interfaces couple together, and pinch.

There has been some recent work by Siegel[24] that extends Moore's analysis of the Kelvin–Helmholtz instability and includes the effect of surface tension. While his work predicts the formation of corner singularities in the sheet profiles, it differs from our results in several important ways. First, the corner singularities found in Siegel's analysis are isolated and are not associated with the formation of a topological singularity. That is, there is *no* pinching. Second, his analysis predicts the formation of such a corner singularity for any value of *We* for which there is an unstable wavelength. We find instead that for moderate *We* with a few unstable modes, the formation of interpenetrating fingers that apparently elongate continuously without interruption by any singularity. Pinching singularities appear only at yet larger values of the Weber number. Finally, Siegel's work apparently predicts the algebraic exponents, associated with the singularity, to be $\psi_\kappa = -1/3$ and $\psi_\gamma = -2/3$. While we did not find very conclusive values for these exponents, our fits do seem well away from these values. However, as Siegel remarks, Moore's approximation often gives incorrect values for temporal exponents, while giving correct results on the spatial form of the singularity.[47] On the qualitative side, the solutions he finds do bear some resemblance to the growing fingers at early times.

As Siegel also remarks, the approximations inherent in his analysis may lose their validity as the singularity time is approached, and so may not capture the interactions necessary to observe pinching. One such interaction that is critical to pinching is the nonlocal coupling, though the Birkhoff–Rott integral, between separated parts of the sheet. Siegel's system is local in space. Another consideration is that Siegel's conclusions are based on specific initial data that correspond to special ''travelling wave'' solutions of his approximate equations. We have not investigated this particular set of initial data.

Very similar pinching singularities have been observed in other situations where the Kelvin–Helmholtz instability is operative. In HLS94, we observed the beginnings of a pinching singularity in plume vortices formed by the Rayleigh–Taylor instability in the Boussinesq approximation (see Fig. 18 there). In a very recent study of the application of SSD methods to water waves and fully density-stratified flows (as in this study, incompressible, inviscid, irrotational, and 2-d), Hou and Ceniceros[37] have also observed such singularities, and measured length collapse exponents very close to 2/3. As has been the case for the basic description of Moore singularity in stratified flow without surface tension,[22] it seems likely to us that the prototype pinching singularity is found in the simplest case of no stratification at all.

An intriguing question is whether ''bubble'' formation as apparently predicted by these calculations, is observable in an experimental setting. In Ref. 48, Thorpe presents an experimental study of the development of the K–H instability in a sharply stratified shear flow between two nearly immiscible fluids. Of course, in such an experimental situation there are many additional effects, such as viscosity, three-dimensionality, and partial miscibility, that we have neglected in our model. However, Thorpe does remark that the interface between the two fluids ''became very irregular, sometimes being broken and drops of one fluid being produced in the other, … .'' The effects of additional physics are currently being considered in other works, see Refs. 49–54, for example. While these additional effects could certainly play an important role in determining the overall structure of the flow, there is no doubt that topological transitions/singularities are a fundamental feature of the motion of real fluids. We hope to have suggested one of the simplest settings in which such phenomena occur.

ACKNOWLEDGMENTS

We thank Russ Caflisch, Ray Goldstein, Joe Keller, Dan Meiron, and Mary Pugh for important conversations. T.Y.H. acknowledges support from National Science Foundation (NSF) Grant No. DMS-9407030, Office of Naval Research Grant No. N00014-94-1-0310, and Department of Energy Grant No. DE-FG03-89ER25073. J.S.L. acknowledges the support from NSF Grant No. DMS-9404310, the Sloan Foundation, the McKnight Foundation, and the Minnesota Supercomputer Institute. M.J.S. acknowledges support from Department of Energy Grant No. DE-FG02-88ER25053, National Science Foundation Grants No. DMS-9396403 (PYI) and No. DMS-9404554, and the Exxon Educational Foundation.

APPENDIX A: CONSTRUCTING THE NONUNIFORM MESH MAPPING

As described in our previous paper,[2] the construction of the nonuniform mesh requires a scaling function R. Suppose that α is the uniform parametrization variable. We introduce a new parametrization β such that $\alpha = \alpha(\beta)$ and that $R(\beta) = \alpha_\beta$ is small in regions where the interface is most singular. This has the effect of clustering grid points since

$$s_\beta(\beta,t) = L(t)R(\beta), \text{ with} \int_0^1 R(\beta')d\beta' = 1, \tag{A1}$$

where $L(t) = \int_0^1 s_{\beta'} d\beta'$ is the total arclength of the interface at time t.

Suppose first that the interface is most singular near a single region centered around $\alpha = \alpha_c$. Then, one natural choice for R is to set $R(\beta)$ to be a step function which takes a small value near $\beta = \beta_c$, where $\alpha(\beta_c) = \alpha_c$. The relationship between α and β is given by

$$\alpha(\beta)=\int_0^\beta R(\beta')d\beta', \tag{A2}$$

which maps the unit interval $[0,1]$ onto itself. Since R is chosen to be positive, the mapping is strictly monotone. Therefore the inverse always exists. In general, before we construct R, we do not know how β_c relates to α_c. However, when R is a step function, there is an explicit relationship between the two. For example, choose R to be the following step function satisfying $R(\beta)=R_{min}$ for $\beta \in [\beta_c-\delta,\beta_c+\delta]$, and $R(\beta)=R_{max}$ otherwise. Given R_{min} and δ, R_{max} is uniquely determined by satisfying $\int_0^1 R(\beta)d\beta=1$. This gives $R_{max}=(1-2\delta R_{min})/(1-2\delta)$. Moreover, using (A2) and the relationship $\alpha(\beta_c)=\alpha_c$, we obtain the explicit formula relating β_c to α_c:

$$\beta_c=\delta+(\alpha_c-\delta R_{min})/R_{max}. \tag{A3}$$

However, choosing R to be a step function does not provide a smooth enough parametrization for our numerical simulations. Therefore, we actually obtain R by smoothing the above step function by convolving it with the heat kernel. This amounts to diffusing the step function for the short time t_Δ. Since this diffusion does not change the mean of a function and only slightly changes the position of its local extrema, the above formula for β_c remains valid.

We can easily generalize this idea for the case in which local mesh refinement is required for more than one region. For example, consider a refinement in regions centered around $\alpha_{c,1}$ and $\alpha_{c,2}$. Define $R(\beta)=R_{min}$ for $\beta \in [\beta_{c,1}-\delta,\beta_{c,1}+\delta]$ and $\beta \in [\beta_{c,2}-\delta,\beta_{c,2}+\delta]$, and $R(\beta)=R_{max}$ otherwise. Then, the explicit formulae for $\beta_{c,1}$ and $\beta_{c,2}$ are

$$\beta_{c,1}=\delta+(\alpha_{c,1}-\delta R_{min})/R_{max},$$

$$\beta_{c,2}=3\delta+(\alpha_{c,2}-3\delta R_{min})/R_{max}.$$

In our simulations, we used $\delta=0.05$, $R_{min}=0.06$, and $t_\Delta=0.005$. After the diffusion process, the minimum value of R is about 0.1 in a small neighborhood of the β_c. This gives approximately 8 more points near the local singular region. To find the α_c, we ran the uniform parametrization calculation and determined where the local maxima of the curvature, or the minima of the pinching distance, occur. Finally, once R is constructed as above, the grid mapping $\alpha_j=\alpha(\beta_j)$, where $\beta_j=jh$ is found using a spectral approximation of the integral in (A2). Spectral interpolation is also used to obtain the values of the interface quantities on the new grid $\{\alpha_j\}_{j=1}^N$.

APPENDIX B: TIME-INTEGRATION METHODS

The time-integration scheme we used in this paper, for the $We=200$ simulation, is a fourth-order multi-step implicit/explicit scheme studied in Ref. 35 by Ascher, Ruuth, and Wetton. Consider a time-dependent PDE in which the spatial derivatives have been discretized by either central differences or by spectral or pseudo-spectral methods. This gives rise to a large system of ODEs in time which typically has the form

$$\frac{du}{dt}=f(u)+\nu g(u), \tag{B1}$$

where g is a linear operator containing high-order derivatives and $f(u)$ is a nonlinear function which we do not want to integrate implicitly in time. To avoid using excessively small time steps, we would like to treat the $\nu g(u)$ term implicitly while treating the nonlinear term $f(u)$ explicitly. Typically, $f(u)$ involves only first-order derivatives from convective terms, so the stiffness induced from the nonlinear term is not as severe as that from the linear operator $g(u)$.

A straightforward implicit/explicit time integration scheme is to use the second-order Adams–Bashforth scheme for the explicit term and the Crank–Nicholson scheme for the implicit term. This gives

$$\frac{u^{n+1}-u^n}{\Delta t}=\frac{3}{2}f(u^n)-\frac{1}{2}f(u^{n-1})+\frac{\nu}{2}[g(u^{n+1})+g(u^n)], \tag{B2}$$

where Δt is the time step size and u^n is the numerical approximation to $u(n\Delta t)$. In general, one can construct a family of high-order implicit/explicit schemes based Taylor expansions. However, they do not all share the same stability properties.

The fourth-order implicit/explicit scheme considered by Ascher, Ruuth, and Wetton seems to be quite stable. The scheme is given as follows:

$$\frac{1}{\Delta t}\left(\frac{25}{12}u^{n+1}-4u^n+3u^{n-1}-\frac{4}{3}u^{n-2}+\frac{1}{4}u^{n-3}\right) \tag{B3}$$

$$=4f(u^n)-6f(u^{n-1})+4f(u^{n-2})-f(u^{n-3})+\nu g(u^{n+1}). \tag{B4}$$

For example, if $f(u)=au_x$, $g(u)=u_{xx}$, and a spectral discretization is used in space, then a von-Neumann stability analysis shows that the scheme is stable for $\Delta t \leqslant 0.52h/a$.[35]

We now apply this fourth-order implicit/explicit scheme to our problem,

$$\theta_t=\frac{1}{2s_\alpha}\left(\frac{1}{s_\alpha}H(\gamma)\right)_\alpha+P, \tag{B5}$$

$$\gamma_t=-S\left(\frac{\theta_\alpha}{s_\alpha}\right)_\alpha+Q, \tag{B6}$$

where P and Q are the nonlinear terms. We obtain the following system:

$$\frac{1}{\Delta t}\left(\frac{25}{12}\theta^{n+1}-4\theta^n+3\theta^{n-1}-\frac{4}{3}\theta^{n-2}+\frac{1}{4}\theta^{n-3}\right)$$

$$=\frac{1}{2s_\alpha^{n+1}}\left(\frac{1}{s_\alpha^{n+1}}H(\gamma^{n+1})\right)_\alpha+4P^n-6P^{n-1}+4P^{n-2}-P^{n-3}$$

and

$$\frac{1}{\Delta t}\left(\frac{25}{12}\gamma^{n+1}-4\gamma^{n}+3\gamma^{n-1}-\frac{4}{3}\gamma^{n-2}+\frac{1}{4}\gamma^{n-3}\right)$$
$$=S\left(\frac{\theta_\alpha^{n+1}}{s_\alpha^{n+1}}\right)_\alpha+4Q^n-6Q^{n-1}+4Q^{n-2}-Q^{n-3}.$$

By substituting γ^{n+1} into the equation for θ^{n+1}, we can eliminate γ^{n+1} and obtain a single equation for θ^{n+1}, which takes the form

$$s_\alpha^{n+1}\theta^{n+1}-\frac{S}{2}\left(\frac{12}{25}\right)^2\Delta t^2\left(\frac{1}{s_\alpha^{n+1}}H\left[\frac{\theta_\alpha^{n+1}}{s_\alpha^{n+1}}\right]_\alpha\right)_\alpha=N(\alpha), \tag{B7}$$

where N is a known quantity depending on the solutions at the previous time steps. The spatial derivative is discretized by a spectral method. In the case of uniform parametrization formulation, s_α is independent of α. In this case, the operator in the left hand side of (B7) is a linear constant coefficient operator which is diagonalized by the Fourier transform. Therefore, in the uniform case, we solve for θ^{n+1} explicitly using the Fast Fourier transform (FFT). However, when the variable parametrization frame is used, s_α^{n+1} depends on α and so the equation is no longer diagonalized by the Fourier transform. Consequently, in the variable case, we use an iterative method to solve for θ^{n+1}. Note that the linear operator in the left hand side of (B7) is symmetric, positive definite. Thus, we use the preconditioned conjugate gradient method to solve for θ^{n+1}. The preconditioning operator M is given by

$$M(\theta^{n+1})=s_{max}\theta^{n+1}-\frac{S}{2s_{min}^2}\left(\frac{12}{25}\right)^2\Delta t^2(H[\theta_\alpha^{n+1}]_\alpha)_\alpha, \tag{B8}$$

where $s_{min}=\min_\alpha s_\alpha^{n+1}$ and $s_{max}=\max_\alpha s_\alpha^{n+1}$. Thus, M is a constant coefficient and is diagonalized by the Fourier transform:

$$\widehat{M(\theta)}(k)=\left(s_{max}+\frac{S}{2s_{min}^2}\left(\frac{12}{25}\right)^2\Delta t^2|k|^3\right)\hat{\theta}(k). \tag{B9}$$

So, inverting M only requires $N\log(N)$ operations using the FFT. We also use the solutions from the previous four time steps to extrapolate a fourth-order initial guess for θ^{n+1}. Typically it takes a few iterations to converge with an iterative error of 1×10^{-11} until very close to the singularity time.

APPENDIX C: THE CONSEQUENCES OF INTERFACE COLLISION

We show that the collision (or self-intersection) of material surfaces, such as vortex sheets, corresponds to a true fluid dynamic singularity. In particular, if $\Omega(t)$ is any material volume (or area) *strictly between* the colliding material surfaces, then

$$\int_0^t\|\nabla\mathbf{u}(\cdot,t')\|_{L^\infty(\Omega(t'))}dt'\to\infty,\quad as\quad t\to t_c, \tag{C1}$$

where t_c is the time that the collision occurs. Thus, the strain rates diverge in a pointwise sense and must do so at least as rapidly as $1/(t_c-t)$. As will be shown in section IV, the singularity we observe is accompanied by the blow-up of the fluid velocity itself which assures (C1) is satisfied. The proof of Eq. (C1) is straightforward and we sketch it briefly here. Let ξ be a smooth scalar field on $\Omega(0)$ taking the value 1 on one of the colliding surfaces and 0 on the other. Let ξ be advected by the fluid velocity $\mathbf{u}$. Then, it can be shown that

$$\|\nabla\xi(\cdot,t)\|_{L^2(\Omega(t))}\leq\|\nabla\xi(\cdot,0)\|_{L^2(\Omega(0))}\times\exp\left[\int_0^t\|\nabla\mathbf{u}(\cdot,t')\|_{L^\infty(\Omega(t'))}dt'\right]. \tag{C2}$$

Using the mean value theorem for integrals and incompressibility, one obtains

$$|\nabla\xi(\mathbf{x}_0,t)|\leq\|\nabla\xi(\cdot,0)\|_{L^\infty(\Omega(0))}\times\exp\left[\int_0^t\|\nabla\mathbf{u}(\cdot,t')\|_{L^\infty(\Omega(t'))}dt'\right], \tag{C3}$$

for some $\mathbf{x}_0\in\Omega(t)$. Since this is true for any material domain $\Omega(t)$ and since $|\nabla\xi|\to\infty$ at the collision point, Ω can be taken sufficiently localized about the collision point so that $|\nabla\xi(\mathbf{x}_0,t)|$ becomes arbitrarily large as $t\to t_c$, the collision time.

[1] P. G. Saffman and G. R. Baker, ''Vortex interactions,'' Annu. Rev. Fluid Mech. **11**, 95 (1979).

[2] T. Hou, J. Lowengrub, and M. Shelley, ''Removing the stiffness from interfacial flows with surface tension,'' J. Comput. Phys. **114**, 312 (1994).

[3] Lord Rayleigh, ''On the instability of jets,'' Proc. London Math. Soc. **10**, 4 (1879).

[4] H. A. Stone and L. G. Leal, ''Relaxation and breakup of an initially extended drop in an otherwise quiescent fluid,'' J. Fluid Mech. **198**, 399 (1989); M. Tjahjadi, H. A. Stone, and J. M. Ottino, ''Satellite and subsatellite formation in capillary breakup,'' J. Fluid Mech. **243**, 297 (1992).

[5] S. Tanveer and G. L. Vasconcelos, ''Bubble breakup in two-dimensional Stokes flow,'' Phys. Rev. Lett. **73**, 2845 (1994).

[6] A. L. Bertozzi, M. P. Brenner, T. F. Dupont, and L. P. Kadanoff, ''Singularities and similarities in interface flows,'' in *Trends and Perspectives in Applied Mathematics*, edited by L. Sirovich (Springer-Verlag Applied Mathematics Series, New York, 1994).

[7] P. Constantin, T. F. Dupont, R. E. Goldstein, L. P. Kadanoff, M. Shelley, and S.-M. Zhou, ''Droplet breakup in a model of the Hele-Shaw cell,'' Phys. Rev. E **47**, 4169 (1993); T. F. Dupont, R. E. Goldstein, L. P. Kadanoff, and S.-M. Zhou, ''Finite-time singularity formation in Hele-Shaw systems,'' *ibid.* **47**, 4182 (1993).

[8] R. Goldstein, A. Pesci, and M. Shelley, ''Topology transitions and singularities in viscous flows,'' Phys. Rev. Lett. **70**, 3043 (1993). Also, R. Goldstein, A. Pesci, and M. Shelley, ''Attracting manifold for a viscous topology transition,'' Phys. Rev. Lett. **75**, 3665 (1995).

[9] R. Almgren, A. Bertozzi, and M. Brenner, ''Stable and unstable singularities in the unforced Hele-Shaw cell,'' Phys. Fluids A **8**, 1356 (1996).

[10] S. Cardoso and A. Wood, ''The formation of drops through viscous instability,'' J. Fluid Mech. **289**, 351 (1995).

[11] R. Almgren, ''Singularity formation in Hele-Shaw bubbles,'' Phys. Fluids A **8**, 344 (1996).

[12] J. Eggers, ''Universal pinching of 3D axisymmetric free-surface flow,'' Phys. Rev. Lett. **71**, 3458 (1993); J. Eggers and T. F. Dupont, ''Drop formation in a one-dimensional approximation of the Navier–Stokes equation,'' J. Fluid Mech. **262**, 205 (1994).

[13] X. D. Shi, M. P. Brenner, and S. R. Nagel, ''A cascade of structure in a drop falling from a faucet,'' Science **265**, 219 (1994); M. P. Brenner, X. D. Shi, and S. R. Nagel, ''Iterated instabilities during droplet formation,'' Phys. Rev. Lett. **73**, 3391 (1994).

[14] S. Bechtel, C. D. Carlson, and M. G. Forest, ''Recovery of the Rayleigh capillary instability from slender 1-D inviscid and viscous models,'' Phys. Fluids A **12**, 2956 (1995).

[15]J. B. Keller and M. Miksis, ''Surface tension driven flows,'' SIAM J. Appl. Math **43**, 268 (1983).
[16]D. Moore, ''The spontaneous appearance of a singularity in the shape of an evolving vortex sheet,'' Proc. R. Soc. London Ser. A **365**, 1059 (1979).
[17]R. Caflisch and O. Orellana, ''Singular solutions and ill-posedness of the evolution of vortex sheets,'' SIAM J. Math. Anal. **20**, 293 (1989).
[18]D. I. Meiron, G. R. Baker, and S. A. Orszag, ''Analytic structure of vortex sheet dynamics. Part 1. Kelvin–Helmholtz instability,'' J. Fluid Mech. **114**, 283 (1982).
[19]R. Krasny, ''A study of singularity formation in a vortex sheet by the point vortex approximation,'' J. Fluid Mech. **167**, 65 (1986).
[20]M. Shelley, ''A study of singularity formation in vortex sheet motion by a spectrally accurate vortex method,'' J. Fluid Mech. **244**, 493 (1992).
[21]D. A. Pugh, ''Development of vortex sheets in Boussinesq flows— Formation of singularities,'' Ph.D. thesis, Imperial College, London, 1989.
[22]G. Baker, R. Caflisch, and M. Siegel, ''Singularity formation during the Rayleigh–Taylor instability,'' J. Fluid Mech. **252**, 51 (1993).
[23]D. D. Joseph, T. Y. J. Liao, and J.-C. Saut, ''Kelvin–Helmholtz mechanism for side branching in the displacement of light with heavy fluid under gravity,'' Eur. J. Mech. B Fluids **11**, 253 (1992).
[24]M. Siegel, ''A study of singularity formation in the Kelvin–Helmholtz instability with surface tension,'' SIAM J. Appl. Math. **55**, 865 (1995).
[25]G. Baker and A. Nachbin, ''Stable methods for vortex sheet motion in the presence of surface tension,'' preprint.
[26]J. T. Beale, T. Y. Hou, and J. S. Lowengrub, ''Convergence of boundary integral methods for water waves with and without surface tension,'' SIAM J. Num. Anal. **33**, 1797 (1996).
[27]J. T. Beale, T. Y. Hou, and J. S. Lowengrub, ''Growth rates for the linear motion of fluid interfaces far from equilibrium,'' Comments Pure Appl. Math. **XLVI**, 1269 (1993).
[28]R. Zalosh, ''Discretized simulation of vortex sheet evolution with buoyancy and surface tension effects,'' AIAA J. **14**, 1517 (1976).
[29]D. I. Pullin, ''Numerical studies of surface tension effects in nonlinear Kelvin–Helmholtz and Rayleigh–Taylor instability,'' J. Fluid Mech. **119**, 507 (1982).
[30]R. Rangel and W. Sirignano, ''Nonlinear growth of the Kelvin–Helmholtz instability: Effect of surface tension and density ratio,'' Phys. Fluids **31**, 1845 (1988).
[31]G. Baker, D. Meiron, and S. Orszag, ''Generalized vortex methods for free-surface flow problems,'' J. Fluid Mech. **123**, 477 (1982).
[32]G. Carrier, M. Krook, and C. Pearson, *Functions of a Complex Variable*, (McGraw-Hill, New York, 1966).
[33]J. T. Beale, T. Y. Hou, and J. S. Lowengrub, ''On the well-posedness of two fluid interfacial flows with surface tension,'' *Singularities in Fluids, Plasmas and Optics*, edited by R. C. Caflisch and G. C. Papanicolaou (Kluwer Academic, London, 1993).
[34]G. B. Whitham, ''A new approach to problems of shock dynamics, Part I: Two-dimensional problems,'' J. Fluid Mech. **2**, 145 (1957).
[35]U. M. Ascher, S. J. Ruuth, and B. Wetton, ''Implicit–explicit methods for time-dependent partial differential equations,'' SIAM J. Num. Anal. **32**, 797 (1995).
[36]A. Sidi and M. Israeli, ''Quadrature methods for periodic singular and weakly singular Fredholm integral equations,'' J. Sci. Comput. **3**, 201 (1988). For a related, but different quadrature approach, see G. Baker, ''Generalized vortex methods for free-surface flows,'' in *Waves on Fluid Interfaces*, edited by R. E. Meyer (Academic Press, New York, (1983).
[37]T. Hou and H. Ceniceros, ''Convergence of a non-stiff boundary integral method for interfacial flows with surface tension,'' to appear in Math. Comput.
[38]G. R. Baker and M. J. Shelley, ''Boundary integral techniques for multi-connected domains,'' J. Comput. Phys. **64**, 112 (1986).
[39]R. Krasny, ''Desingularization of periodic vortex sheet roll-up,'' J. Comput. Phys. **65**, 292 (1986).
[40]G. R. Baker and M. J. Shelley, ''On the connection between thin vortex layers and vortex sheets,'' J. Fluid Mech. **215**, 161 (1990).
[41]G. Tryggvason, W. J. A. Dahm, and K. Sbeih, ''Fine structure of vortex sheet rollup by viscous and inviscid simulation,'' J. Fluid Eng. **113**, 31 (1991).
[42]R. Krasny, ''Viscous simulation of wake patterns,'' in *Proceedings of the NATO ARW on ''Vortex Flows and Related Numerical Methods,''* edited by J. T. Beale, G.-H. Cottet, and S. Huberson, NATO ASI Ser. 395, 1993, p. 145.
[43]R. Caflisch and J. Lowengrub, ''The convergence of the vortex method for vortex sheets,'' SIAM J. Num. Anal. **26**, 1060 (1989).
[44]J.-Y. Chemin, ''Persistance de structures geometriques dans les fluides incompressibles bidimensionnels,'' Ann. Ecole Normale Supérieure **26**, 1 (1993).
[45]A. L. Bertozzi and P. Constantin, ''Global regularity for vortex patches,'' Commun Math. Phys. **152**, 19 (1993).
[46]M. Pugh and M. Shelley, ''Singularity formation in models of thin jets,'' submitted to Commun. Pure Appl. Math.
[47]M. Siegel (private communication).
[48]S. Thorpe, ''Experiments on the instability of stratified shear flows: Immiscible flows,'' J. Fluid Mech. **39**, 25 (1969).
[49]J. S. Lowengrub and L. Truskinovsky, ''Quasi-incompressible Cahn–Hilliard fluids and topological transitions,'' submitted to Proc. R. Soc. London Ser. A.
[50]J. S. Lowengrub, M. J. Shelley, L. Truskinovsky, and J. Goodman, ''Topological transitions in fluid-fluid jets using Cahn–Hilliard hydrodynamics,'' in preparation.
[51]Y. C. Chang, T. Y. Hou, B. Merriman, and S. Osher, ''Eulerian capturing methods based on a level set formulation for incompressible fluid interfaces,'' J. Comput. Phys. **124**, 449 (1996).
[52]M. Sussman, P. Smereka, and S. Osher, ''A level set approach for computing solutions to incompressible two-phase flow,'' J. Comput. Phys. **114**, 146 (1994).
[53]J. U. Brackbill, D. B. Kothe, and C. Zemach, ''A continuum method for modeling surface tension,'' J. Comput. Phys. **100**, 335 (1992).
[54]M. E. Gurtin, D. Polignone, and J. Vinals, ''Two-phase binary fluids and immiscible fluids described by an order parameter,'' to appear in Math. Mod. Methods Appl. Sci.